MOX-Report No. 58/2018

A sequential coupling of shape and topology optimization for structural design

Ferro, N.; Micheletti, S.; Perotto, S.

MOX, Dipartimento di Matematica
Politecnico di Milano, Via Bonardi 9 - 20133 Milano (Italy)

mox-dmat@polimi.it http://mox.polimi.it

A sequential coupling of shape and topology optimization for structural design

Nicola Ferro[#], Stefano Micheletti[#], Simona Perotto[#]

November 6, 2018

[#] MOX– Modellistica e Calcolo Scientifico
Dipartimento di Matematica, Politecnico di Milano
Piazza L. da Vinci 32, I-20133 Milano, Italy
{nicola.ferro,stefano.micheletti,simona.perotto}@polimi.it

Abstract

We consider different algorithms to design lightweight and stiff structures exhibiting free-form features. First we apply a shape optimization and a topology optimization procedure, separately. Then, we couple these two techniques sequentially. Topology optimization is also enhanced by a structure-tailored computational mesh, made it possible by anisotropic mesh adaptation. This allows us to obtain an intrinsically smooth final layout which can be directly moved on to the production manufacturing phase. An extensive numerical assessment corroborates both qualitatively and quantitatively the performances of the proposed algorithms.

1 Introduction

The spreading of new manufacturing technologies has prompted new paradigms for designing structures. In particular, Additive Layer Manufacturing (ALM) has allowed the production of objects without many of the geometrical and manufacturability constraints imposed by traditional technologies, such as material removal, forming and tooling. Both traditional and innovative technologies can be driven by trial-and-error or more rigorous optimization procedures which aim at identifying an optimal material distribution within a given design domain, according to prescribed requirements. This paper focuses on sophisticated mathematical methods, namely Shape Optimization and Topology Optimization (see, e.g., [1, 2, 3, 4, 5, 6, 7, 8, 9, 10]). A third possible technique is represented by Size Optimization which is, however, not considered here, being less effective with respect to the others.

Shape and topology optimization pursue the common goal of minimizing a certain cost functional, under given constraints on mass, stiffness or other physical quantities of interest related to the application at hand. However,

they work in a complementary way. Shape optimization modifies the design domain by changing its boundary, while preserving the topology; on the contrary, topology optimization allows one to change the topology of the final structure, preserving the outer boundary of the original domain but enforcing a given reduction of the mass. Thus, the final structure may have a completely different layout with respect to the starting one, including regions of void of arbitrary shape, according to a free-form design [11, 12].

In this paper, we tackle the minimum compliance problem in the linear elastic case (see, e.g., [3, 13, 14, 15]). In more detail, we seek the optimal structure, $\Omega \subset \mathbb{R}^3$, minimizing the static compliance under assigned design constraints and loads. We assume that a load, $\mathbf{f} : \Gamma_N \to \mathbb{R}^3$, is applied on a portion Γ_N of the boundary, $\partial\Omega$, of the structure. Then, the compliance is given by

$$\mathcal{G}(\mathbf{u}) = \int_{\Gamma_N} \mathbf{f} \cdot \mathbf{u}\, d\gamma,$$

with $\mathbf{u} = (u_1, u_2, u_3)^T : \Omega \to \mathbb{R}^3$ the induced displacement field. From a physical viewpoint, $\mathcal{G}$ corresponds to the work done by the external forces. The minimization of this work is equivalent to the maximization of the structure stiffness.

The linear elasticity problem represents the mathematical model underlying the structure deformation [16], and is given by

$$\begin{cases} -\nabla \cdot \sigma(\mathbf{u}) = \mathbf{0} & \text{in } \Omega \\ \mathbf{u} = \mathbf{0} & \text{on } \Gamma_D \\ \sigma(\mathbf{u})\mathbf{n} = \mathbf{f} & \text{on } \Gamma_N \\ \sigma(\mathbf{u})\mathbf{n} = \mathbf{0} & \text{on } \Gamma_F, \end{cases} \tag{1}$$

where $\sigma(\mathbf{u}) = 2\mu\varepsilon(\mathbf{u}) + \lambda I : \varepsilon(\mathbf{u})$ is the stress tensor for an isotropic material, with $\varepsilon(\mathbf{u}) = \left(\nabla\mathbf{u} + (\nabla\mathbf{u})^T\right)/2$ the small displacement strain tensor,

$$\lambda = \frac{E\nu}{(1+\nu)(1-2\nu)}, \quad \mu = \frac{E}{2(1+\nu)}$$

are the Lamé coefficients, with E the Young modulus, ν the Poisson ratio and I the identity tensor, $\mathbf{n}$ is the unit outward normal vector to $\partial\Omega$, Γ_D is the portion of the boundary where homogeneous Dirichlet conditions are imposed (i.e., where the structure is clamped), and Γ_F is the normal stress-free boundary, such that $\Gamma_D \cup \Gamma_N \cup \Gamma_F = \partial\Omega$.

From a numerical viewpoint, the discretization is performed via a standard finite element technique. Hence, we derive the weak form of system (1),

find $\mathbf{u} \in U = \{\mathbf{v} \in [H^1(\Omega)]^3 \ : \ \mathbf{v} = \mathbf{0} \text{ on } \Gamma_D\}$, such that

$$a(\mathbf{u}, \mathbf{v}) = \mathcal{G}(\mathbf{v}) \quad \forall \mathbf{v} \in U, \tag{2}$$

with

$$a(\mathbf{u},\mathbf{v}) = \int_\Omega \sigma(\mathbf{u}) : \varepsilon(\mathbf{v})\, d\Omega, \quad \mathcal{G}(\mathbf{v}) = \int_{\Gamma_N} \mathbf{f}\cdot\mathbf{v}\, d\gamma.$$

In this work, we numerically address the structural optimization problem by means of both shape and topology optimization, highlighting pros and cons of the two techniques. In particular, in order to increase the performances of standard topology optimization algorithms, we enrich a classical density-based approach with an anisotropic mesh adaptation procedure [17, 18]. In addition to the separate analysis of the two optimization techniques, we couple them sequentially, aiming at taking advantage of their specific features (see, e.g., [19, 20, 21, 22, 23]).

The paper is organized as follows. In Section 2, we provide some basic elements of shape optimization, with particular attention to the definition of shape derivative and to some implementation issues. Section 3 is devoted to topology optimization. A standard density-based approach is presented and combined with an anisotropic mesh adaptation procedure. Then, in Section 4, the shape and topology optimization algorithms are combined and numerically assessed. Finally, we draw some conclusions and highlight possible future developments.

2 Shape optimization

Shape optimization (SO) pursues the minimization of a functional of interest, $\mathcal{J}$, through a change in the shape of the domain alone, without modifying the topology and the volume of the initial configuration, Ω^0. Thus, the SO problem is

find $\Omega^{OPT} \in \mathcal{U}_{ad}$ such that

$$\mathcal{J}(\Omega^{OPT}) = \min_{\Omega\in\mathcal{U}_{ad}} \mathcal{J}(\Omega),$$

where $\mathcal{U}_{ad}$ is the set of all the admissible domains $\Omega \subset \mathbb{R}^3$.

We distinguish shape optimization into two categories, according to the method employed to modify the boundaries of the domain [1, 24, 25]. In particular, it is possible to express the shape in terms of a small number, N, of parameters. Hence, any modification of Ω can be represented by the variations of such parameters. In this case, we refer to the method as to *parametrized shape optimization*. Although this method is easy to implement and essentially relies on solving N equations, it turns out to be little handy due to the few possible choices in varying the shape. On the contrary, *geometric shape optimization* allows more freedom since it does not restrict a priori the set of possible deformations. Following this approach, $\partial\Omega$ has to be considered as the design variable. Due to its higher flexibility, we focus on the geometric technique.

2.1 The shape derivative

In order to derive the SO algorithm, we briefly examine the gradient method in a Hilbert space, X, [26, 27]. In the context of the minimization of a functional, $\mathcal{J}$, the gradient method consists in updating the current design variable, $\mathbf{x}^k$, along a descent direction, $\mathbf{d}^k$, so that

$$\mathbf{x}^{k+1} = \mathbf{x}^k - \ell^k \mathbf{d}^k, \tag{3}$$

where $\ell^k \in \mathbb{R}^+$ properly tunes the length of the descent step. Vector $\mathbf{d}^k$ identifies the best direction to minimize the functional, and it is related to the gradient, $\mathcal{J}'$, of $\mathcal{J}$, by

$$(\mathbf{d}^k, \theta)_X = {}_{X^*}\!<\mathcal{J}', \theta>_X \quad \forall \theta \in X, \tag{4}$$

$(\cdot,\cdot)_X$ being the inner product in X and ${}_{X^*}\!<\cdot,\cdot>_X$ the duality pairing between X and its dual, X^*. As a result, for a suitably small step size ℓ^k, $\mathbf{d}^k$ is a descent direction and $\mathcal{J}(\mathbf{x}^{k+1}) < \mathcal{J}(\mathbf{x}^k)$.
Additionally, in the case of a functional $\mathcal{J}$ strongly convex, it holds that

$$\mathbf{x}^k \xrightarrow[k\to+\infty]{} \mathbf{x}^* = \arg\min_{\mathbf{x}\in X} \mathcal{J}(\mathbf{x}).$$

With reference to the shape optimization problem, we employ the Hadamard boundary variation method to account for modifications of the domain Ω [8, 28, 29, 30], and we endow $\mathcal{U}_{ad} \subset \mathbb{R}^3$ with a differentiable structure.
Given a vector field $\theta : \Omega \subset \mathbb{R}^3 \to \mathbb{R}^3$, $\theta \in W^{1,\infty}(\mathbb{R}^3, \mathbb{R}^3)$, a generic variation of Ω can be indicated as

$$\Omega(\theta) = (I + \theta)\Omega = \{\mathbf{x} + \theta(\mathbf{x}) | \mathbf{x} \in \Omega\}.$$

It holds

Lemma 2.1 *For $\theta \in W^{1,\infty}(\mathbb{R}^3, \mathbb{R}^3)$ such that $||\theta||_{W^{1,\infty}(\mathbb{R}^3,\mathbb{R}^3)} < 1$, the map $(I + \theta)$ is a Lipschitz diffeomorphism.*

A scalar function $\Omega \mapsto \mathcal{J}(\Omega) \in \mathbb{R}$ is shape differentiable at Ω if the function $\mathcal{J}_\Omega : \theta \mapsto \mathcal{J}(\Omega(\theta))$ is Fréchet-differentiable at 0, provided that $\theta \in W^{1,\infty}(\mathbb{R}^3, \mathbb{R}^3)$ and Ω is a smooth domain. In particular,

$$\mathcal{J}(\Omega(\theta)) = \mathcal{J}(\Omega) + \mathcal{J}'(\Omega)(\theta) + o(||\theta||_{W^{1,\infty}(\mathbb{R}^3,\mathbb{R}^3)}).$$

We refer to the linear mapping $\theta \mapsto \mathcal{J}'(\Omega)(\theta)$ as to the *shape derivative* of $\mathcal{J}$ at Ω [8, 28, 29, 30]. Then, the descent direction, $\mathbf{d}$, is computed by solving a regularized version of (4), i.e., as the unique solution to the following boundary value problem,

find $\mathbf{d} \in [H^1(\Omega)]^3$ such that

$$\int_\Omega (\nabla \mathbf{d} \cdot \nabla \theta + \mathbf{d} \cdot \theta) d\Omega = (\mathcal{J}'(\Omega), \theta) \quad \forall \theta \in [H^1(\Omega)]^3,$$

$(\cdot,\cdot)$ being the standard inner product in $[H^1(\Omega)]^3$.

2.1.1 The shape derivative in the minimum compliance problem

We define $\mathcal{U}_{ad} = \{A \subset \mathbb{R}^3 \,|\, \Gamma_N \cup \Gamma_D \subset \partial A, |A| = V_0\}$, with $|\cdot|$ the measure of an open set and V_0 a prescribed volume for the admissible shape.
Thus, the definition of shape derivative for the minimum compliance problem can be formulated.

Proposition 2.1 *Let Ω be a smooth bounded open set in $\mathbb{R}^3$ and $\theta \in [H^1(\Omega)]^3$ and assume that the solution to (1) belongs to $[H^2(\Omega)]^3$. Then, the shape derivative of $\mathcal{G}(\Omega)$ is*

$$(\mathcal{G}'(\Omega), \theta) = -\int_{\Gamma_F} \left[2\mu\|\epsilon(\boldsymbol{u})\|^2 + \lambda[\nabla \cdot \boldsymbol{u}]^2\right](\theta \cdot \boldsymbol{n}) d\gamma,$$

where Γ_F is the portion of the boundary allowed to change and $\|\cdot\|$ denotes the tensor norm.

We define the set $\mathcal{D} = \{\delta \in [H^1(\Omega)]^3 |\ \delta = 0 \text{ on } \Gamma_D \cup \Gamma_N\}$ of the possible descent directions [30, 31]. Then, the optimal descent direction for the gradient method solves the problem

find $\mathbf{d} \in \mathcal{D}$ such that

$$\begin{aligned}&\int_\Omega (\nabla \mathbf{d} \cdot \nabla \theta + \mathbf{d} \cdot \theta) d\Omega = \\ &-\int_{\Gamma_F} \left[(2\mu\|\epsilon(\mathbf{u})\|^2) + \lambda[\nabla \cdot \mathbf{u}]^2\right](\theta \cdot \mathbf{n}) d\gamma \quad \forall \theta \in \mathcal{D}.\end{aligned} \tag{5}$$

2.2 Numerical implementation

For numerical purposes, the SO algorithm is implemented in a finite element code. The discretization is performed on a mesh, $\mathcal{T}_h$, composed by regular tetrahedra and we employ Lagrangian finite elements [32]. Via Galerkin projection, equations (2) and (5) are discretized, yielding

find $\mathbf{u}_h \in U_h^s$, such that

$$a(\mathbf{u}_h, \mathbf{v}_h) = \mathcal{G}(\mathbf{v}_h) \quad \forall \mathbf{v}_h \in U_h^s, \tag{6}$$

for the linear elasticity equation, and

find $\mathbf{d}_h \in \mathcal{D}_h^m$ such that

$$\begin{aligned}&\int_\Omega (\nabla \mathbf{d}_h \cdot \nabla \theta_h + \mathbf{d}_h \cdot \theta_h) d\Omega = \\ &-\int_{\Gamma_F} \left[(2\mu\|\epsilon(\mathbf{u}_h)\|^2) + \lambda[\nabla \cdot \mathbf{u}_h]^2\right](\theta_h \cdot \mathbf{n}) d\gamma \quad \forall \theta_h \in \mathcal{D}_h^m,\end{aligned} \tag{7}$$

for the descent direction computation, where U_h^s and $\mathcal{D}_h^m$ denotes the finite element subspace of U and $\mathcal{D}$ and of degree s and m, respectively. In particular, in the numerical assessment in Section 2.3, we choose $s = m = 1$.

The constraint for the volume is enforced using a Lagrangian approach [33, 30]. We require that the volume, V_0, of the initial domain Ω^0 is preserved in the optimization iterations. To this end, we introduce a positive Lagrange multiplier, ϕ, so that the Lagrangian is

$$\tilde{\mathcal{G}}(\Omega) = \mathcal{G}(\Omega) + \phi\,(V(\Omega) - V_0)\,,$$

where $V(\Omega)$ denotes the volume of the current shape Ω, while ϕ enforces the constraint in a weak sense, and it is changed at each iteration by considering the optimality condition, $\mathcal{G}'(\Omega) + \bar{\phi}V'(\Omega) = 0$, understood in an average sense on the boundary of Ω, solved for $\bar{\phi}$. Following [30], at the k-th iteration, ϕ^{k+1} is thus updated as

$$\phi^{k+1} = \frac{\phi^k + \bar{\phi}}{2} + \varepsilon_\phi \frac{V(\Omega) - V_0}{V_0}, \tag{8}$$

where ε_ϕ is a positive real number, set to 2 in the simulations below.

As far as the update of the computational domain is concerned, we employ rule (3) after identifying the vector $\mathbf{x}^k$ with the vector collecting all of the coordinates of mesh vertices and picking ℓ^k so that functional $\mathcal{G}$ is minimized and no element inversion occurs [7]. We enrich these criteria with the following additional strategy: if $(\mathbf{d}_h^{k+1}, \mathbf{d}_h^k) > 0$, namely two consecutive descent directions are, in some sense, close, we are allowed to choose $\ell^{k+1} > \ell^k$, without compromising the procedure. Conversely, if $(\mathbf{d}_h^{k+1}, \mathbf{d}_h^k) < 0$, the step size is reduced to avoid oscillations in the convergence history. Eventually, a regularization loop over the elements completes the whole process.

The complete procedure is provided in Algorithm 1.

The input parameters to the algorithm are: `kmax` for the maximum number of iterations allowed for the gradient method, Δ_{BEST} a safety factor used to reasonably ensuring convergence to a minimum, $\mathcal{T}_h^0$ the initial mesh, and V_0 for the volume constraint. In lines 6 and 9, `movemesh` is the routine employed to update the current mesh, whereas `regularize` in line 10 performs the tetrahedra regularization. Algorithm 1 has been implemented in the FreeFem++ environment [34].

2.3 Numerical assessment for SO

We carry out three test cases, i.e., the bridge, the cantilever beam, and the dome. In Figures 1, 3, 5, the domain Ω^0 and the load are sketched. In particular, we mark with a triangle the portions of surface corresponding to Γ_D, while Γ_N is enclosed within the white boxes. The red arrows indicate the directions of the applied load. In Table 1, we collect the physical parameters used to describe the homogeneous employed materials.

Concerning parameters `kmax` and Δ_{BEST} of Algorithm 1, we set `kmax` $= 300$ and $\Delta_{BEST} = 5$ in all the test cases.

Algorithm 1 Shape Optimization (SO)

Input : $\texttt{kmax}$, Δ_{BEST}, $\mathcal{T}_h^0$, V_0

Set: $\texttt{k} = 0$, $\texttt{k}_{BEST} = 0$, $\mathcal{T}_{BEST} = \mathcal{T}_h^0$, $\mathcal{G}_{BEST} = \mathcal{G}(\Omega^0)$;
while $\texttt{k} - \texttt{k}_{BEST} < \Delta_{BEST}$ & $\texttt{k} < \texttt{kmax}$ **do**
    Solve (6);
    Solve (7);
    Compute $\phi^{\texttt{k}}$, $\ell^{\texttt{k}}$;
    $\mathcal{T}_h^{\texttt{k}+1} = \texttt{movemesh}(\mathcal{T}_h^{\texttt{k}}, \mathbf{d}_h^{\texttt{k}}, \ell^{\texttt{k}})$;
    while $\mathcal{T}_h^{\texttt{k}+1}$ has degenerate elements **do**
        Reduce $\ell^{\texttt{k}}$;
        $\mathcal{T}_h^{\texttt{k}+1} = \texttt{movemesh}(\mathcal{T}_h^{\texttt{k}}, \mathbf{d}_h^{\texttt{k}}, \ell^{\texttt{k}})$;
    $\mathcal{T}_h^{\texttt{k}+1} = \texttt{regularize}(\mathcal{T}_h^{\texttt{k}+1})$;
    Compute $\mathcal{G}(\Omega)$;
    if $\mathcal{G}(\Omega) < \mathcal{G}_{BEST}$ **then**
        $\mathcal{G}_{BEST} = \mathcal{G}(\Omega)$;
        $\texttt{k}_{BEST} = \texttt{k} + 1$;
        $\mathcal{T}_{BEST} = \mathcal{T}_h^{\texttt{k}+1}$;
    $\texttt{k} = \texttt{k} + 1$;

Test case	E [Pa]	ν [-]
Bridge	15	1/3
Cantilever beam	1.0	1/3
Dome	1.0	1/3

Table 1: Physical parameters employed in the SO simulations.

2.3.1 The bridge test case

We consider the optimization of a simplified bridge, modeled starting from a parallelepiped 6 [m] $\times$1 [m] $\times$1 [m] clamped in four portions of the bottom surface of size 0.01 [m] $\times$0.01 [m] each (see Figure 1, right). The surface load $\mathbf{f} = [0, 0, -1]^T$ is applied onto the rectangular surface 1 [m] $\times$0.1 [m] located at the center of the upper face (see Figure 1, center). The domain Ω^0 is discretized using a tetrahedral mesh composed by 25869 elements.

In Figure 2, the output of the Algorithm 1 is shown at the convergence iteration $\texttt{k} = 33$. The optimized structure preserves the portions Γ_N and Γ_D, as expected and the symmetry of the original configuration.

In Table 2, we collect the value of the compliance for the initial domain and for the optimal structure, and the decreasing percentage of $\mathcal{G}$. The same comparison is carried out on the volume, to assess its conservation. It is remarkable the reduction of $\mathcal{G}$ as well as the almost exact volume conservation.

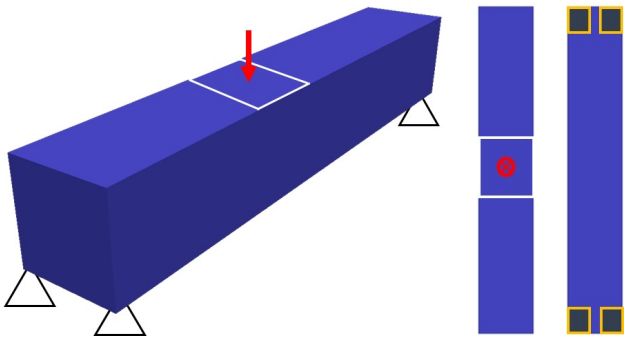

Figure 1: The bridge test case (SO): geometry and boundary conditions (left); details of the top surface, with highlighted Γ_N (white box) and the direction of the load (red marker) (center); details of the bottom surface with highlighted Γ_D (yellow boxes) (right).

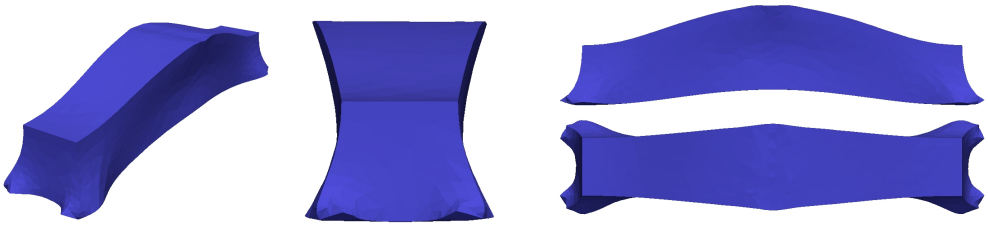

Figure 2: The bridge test case (SO): optimized structure (left), lateral (center), frontal (top-right) and top (bottom-right) views of the optimized structure.

Compliance		
$\mathcal{G}$ before SO	0.0933	[J]
$\mathcal{G}$ after SO	0.0796	[J]
$\Delta_{\%}\mathcal{G}$	-14.68%	[-]

Volume		
V_0	6.000	[m^3]
V after SO	5.999	[m^3]
$\Delta_{\%}V$	-0.017%	[-]

Table 2: The bridge test case (SO): compliance and volume before and after SO.

2.3.2 The cantilever beam test case

We deal with the optimization of a cantilever beam starting from the parallelepiped 2 [m] $\times$1 [m] $\times$0.5 [m] in Figure 3. The entire back face corresponds to Γ_D, Γ_N is a square of side 0.1 [m] centered at the centroid of the frontal face,

and the load $\mathbf{f} = [0, 0, -1]^T$ is tangential to the frontal face. The initial mesh consists of 5870 tetrahedra.

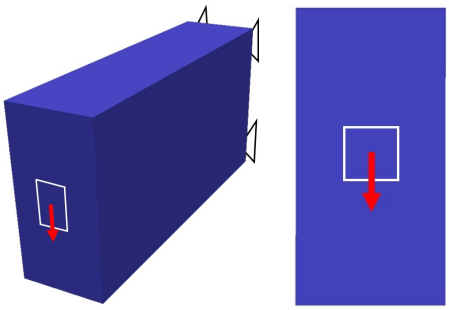

Figure 3: The cantilever beam test case (SO): geometry and boundary conditions (left) and frontal surface (right), with highlighted Γ_N (white box) and the direction of the load (red arrow); the triangles identify Γ_D.

The result of the optimization is shown in Figure 4 after 113 iterations of Algorithm 1. The shape of the new structure is quite different with respect to Ω^0, being more slender in correspondence with the frontal face with respect to the clamped surface. The symmetry is still preserved. From a quantitative

Figure 4: The cantilever test case (SO): optimized structure (left), lateral (center), frontal (top-right) and top (bottom-right) views of the optimized structure.

viewpoint, Table 3 summarizes the compliance and the volume before and after the optimization. In this case, the stiffness of the structure improves strongly, the compliance being reduced of 2/3. Additionaly, also the volume constraint is ensured.

2.3.3 The dome test case

The geometry in Figure 5 is the result of the intersection between a hemispheric shell of radius 1.25 [m], thickness 0.02 [m] and clamped at the bottom, with

Compliance		
$\mathcal{G}$ before SO	0.0309	[J]
$\mathcal{G}$ after SO	0.0104	[J]
$\Delta_{\%}\mathcal{G}$	-66.34%	[-]

Volume		
V_0	1.000	[m^3]
V after SO	1.000	[m^3]
$\Delta_{\%}V$	0.0%	[-]

Table 3: The cantilever beam test case (SO): compliance and volume before and after SO.

a circular cylinder of radius 0.25 [m]. Boundary Γ_N is a portion of the upper surface, concentric to the hole, with radius $0.25 + 0.0314$ [m], and the load is $\mathbf{f} = [0, 0, -1]^T$. The initial spatial discretizion is based on a mesh with 83428 elements.

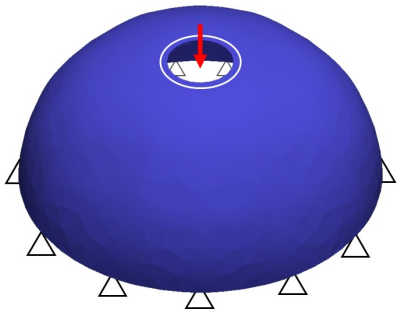

Figure 5: The dome test case (SO): geometry and boundary conditions, with highlighted Γ_N (white circular box) and the direction of the load (red arrow); the triangles identify Γ_D.

We run Algorithm 1 which stops after 198 iterations. The resulting optimized structure is shown in Figure 6. Notice that the initial shape has undergone a sort of squeezing in the vertical direction.

Table 4 collects the values obtained for the compliance and the volume, confirming an enhancement of the mechanical performance of the optimized structure with respect to the original shape.

3 Topology optimization and the SIMP method

One of the most employed mathematical models for topology optimization (TO) is the SIMP (Solid Isotropic Material with Penalization) [35, 3, 36, 37, 38]. Other

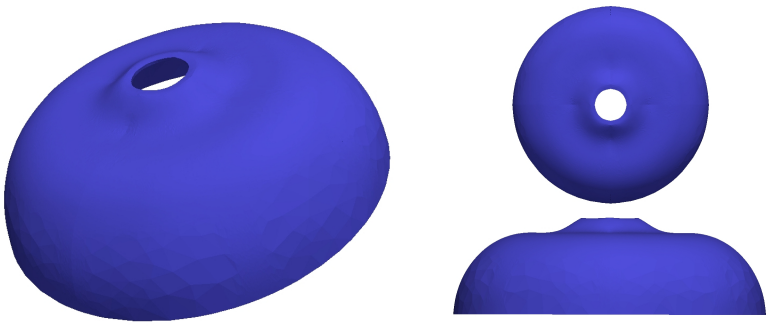

Figure 6: The dome test case (SO): lateral (left), top (top-right) and frontal (bottom-right) views of the optimized structure.

Compliance		
$\mathcal{G}$ before SO	7.1654	[J]
$\mathcal{G}$ after SO	3.2433	[J]
$\Delta_{\%}\mathcal{G}$	-54.74%	[-]

Volume		
V_0	0.05256	[m^3]
V after SO	0.05231	[m^3]
$\Delta_{\%}V$	-0.478%	[-]

Table 4: The dome test case (SO): compliance and volume before and after SO.

approaches exploit level set methods (see, e.g., [33, 39, 40, 41]), homogeneization (see, e.g., [42, 43, 44]), a phase field formulation (see, e.g., [45, 46, 47]), gradient-free methods (see, e.g., [48, 49]), high order discretizations (see, e.g., [50, 51]), cutFEM (see, e.g., [52]) and volumetric expressions of the shape gradient (see, e.g., [53]).

SIMP method is based on an auxiliary variable, ρ, which models the material distribution in the original design domain. In particular, the density function, $\rho \in L^{\infty}(\Omega)$, takes values in $[0, 1]$, where $\rho = 0$ corresponds to the void, whereas $\rho = 1$ identifies the presence of full material. Nevertheless, all the intermediate values in the interval $[0, 1]$ are allowed and for this reason a suitable penalization has to be introduced to push the density to the extremal values, 0 and 1. Thus, the stiffest material and the void are favoured, consistently with the maximization of the structure stiffness. To this end, we employ the standard power law penalization function ρ^p, with $p \geq \max\left\{2/(1-\nu), 4/(1+\nu)\right\}$ [3, 35].

In the minimum compliance framework, model (1) represents the state equation for the optimization problem, after taking into account the material density. In particular, according to the SIMP approach, we solve model (1) with a modified Hooke law with $\rho^p\lambda$ and $\rho^p\mu$ replacing λ and μ, respectively. Thus, the

weak form of the SIMP-linear elasticity equation is

find $\mathbf{u} \in U$ such that

$$a_\rho(\mathbf{u}, \mathbf{v}) = \mathcal{G}(\mathbf{v}) \quad \forall \mathbf{v} \in U, \tag{9}$$

with

$$a_\rho(\mathbf{u}, \mathbf{v}) = \int_\Omega \sigma_\rho(\mathbf{u}) : \varepsilon(\mathbf{v})\, d\Omega,$$

and $\sigma_\rho(\mathbf{u}) = \rho^p \big[2\mu\varepsilon(\mathbf{u}) + \lambda I : \varepsilon(\mathbf{u})\big]$. Notice that $\mathcal{G}(\mathbf{u}) = a_\rho(\mathbf{u}, \mathbf{u})$ still represents the static compliance, i.e., the functional to be minimized.
The topology optimization problem finally becomes

find $\rho \in L^\infty(\Omega)$ such that

$$\min_{\rho \in L^\infty(\Omega)} \mathcal{G}(\mathbf{u}(\rho)) \ : \begin{cases} a_\rho(\mathbf{u}(\rho), \mathbf{v}) = \mathcal{G}(\mathbf{v}) \ \forall \mathbf{v} \in U \\ \int_\Omega \rho \, d\Omega \leq \alpha |\Omega| \\ \rho_{\min} \leq \rho \leq 1, \end{cases} \tag{10}$$

where $0 < \alpha < 1$ denotes the maximum allowable volume fraction and $0 < \rho_{\min} < 1$ is a lower bound for the density, which ensures the elasticity system to be well-defined.

Problem (10) is numerically tackled via a standard finite element discretization. The discrete counterpart of (10) becomes

find $\rho_h \in V_h^r$ such that

$$\min_{\rho_h \in V_h^r} \mathcal{G}(\mathbf{u}_h(\rho_h)) \ : \begin{cases} a_\rho(\mathbf{u}_h(\rho_h), \mathbf{v}_h) = \mathcal{G}(\mathbf{v}_h) \ \forall \mathbf{v}_h \in U_h^s \\ \int_\Omega \rho_h \, d\Omega \leq \alpha |\Omega| \\ \rho_{\min} \leq \rho_h \leq 1, \end{cases} \tag{11}$$

where it is understood that $\mathbf{u}_h(\rho_h) \in U_h^s$ and V_h^r is the finite element space of scalar functions of degree r.

Formulation (11) suffers from two numerical issues, namely the dependence of the final topology on the mesh and the checkerboard effect [3, 50, 54]. The former is linked to the non-uniqueness of the solution to problems (10) and (11). The latter strongly depends on the discretization pair adopted for the density-displacement formulation. It may result in material/void alternation as in a checkerboard, leading to non-manufacturable designs (for additional comments see [17]).

A partial remedy to both mesh dependence and checkerboard effect is to filter the density ρ, with smoothing techniques. Alternatively, it is possible to use higher order finite elements for the displacement with respect to the density ($s \geq r$ in (11)) to tackle the checkerboard issue. However, high order finite elements require a bigger computational effort and this choice may be unaffordable for three dimensional simulations.

As an alternative to these remedies, since the optimized density obtained by the SIMP method exhibits strong gradients in correspondence with the boundaries of the structure (i.e., along the void-material interface), it has been proposed an enrichment of the standard SIMP algorithm with a mesh adaptation strategy in [17]. Among the benefits characterizing this new approach, we mention the possibility to use low degree finite element spaces for both ρ_h and $\mathbf{u}_h$ (i.e., $s = r = 1$) and to avoid a massive employment of filtering, thus containing the computational cost and the post-processing. In particular, we limit the filtering to the very first optimization iteration, when a low-pass filter based on the diffusion kernel is adopted. For this purpose, we replace the density ρ_h with its filtered version, ρ_f, solution to the Helmholtz-type problem

$$\begin{cases} -\tau^2 \Delta \rho_f + \rho_f = \rho_h & \text{in } \Omega \\ \tau^2 \nabla \rho_f \cdot \mathbf{n} = 0 & \text{on } \partial\Omega, \end{cases} \tag{12}$$

with τ a real parameter that measures the characteristic length of the smoothed density [55].

The algorithm merging the SIMP method with the Helmholtz filter for the density is provided in Algorithm 2 [17].

Algorithm 2 SIMP algorithm on a fixed grid

Input : `CTOL`, `kmax`, $\rho_{\min}$

1: Set: $\rho_h^0 = 1$, $\mathtt{k} = 0$, errG = 1+`CTOL`
2: **while** errG > `CTOL` & k < `kmax` **do**
3: $\quad \rho_h^{\mathtt{k}+1} = \mathtt{optimize}(\rho_h^{\mathtt{k}}, \mathtt{Mit}, \mathtt{TOPT}, \nabla_\rho \mathcal{G}, ...)$;
4: $\quad \rho_h^{\mathtt{k}+1} = \rho_f(\rho_h^{\mathtt{k}+1})$;
5: $\quad \text{errG} = \|\rho_h^{\mathtt{k}+1} - \rho_h^{\mathtt{k}}\|_\infty$;
6: $\quad \mathtt{k} = \mathtt{k} + 1$;

Some comments are in order. The main input parameters are the lower value, $\rho_{\min}$, for the density, the maximum number, `kmax`, of iterations and the tolerance `CTOL` for the stopping criterion. In line 3, problem (11) is solved via an optimization routine, i.e., `optimize`. In particular, we employ the Interior Point OPTimizer (IPOPT) package [56], but other options are viable, such as the MMA algorithm [57]. IPOPT is a common large-scale nonlinear optimization tool based on the interior point algorithm [58]. Both equality and inequality constraints can be tackled via suitable slack variables. Constraints may involve both the control variables (for example, the density ρ) as well as functions of these (for instance, the total volume of the structure, $\int_\Omega \rho d\Omega$). Among the input parameters of `optimize`, `Mit` identifies the maximum number of iterations allowed and `TOPT` is the tolerance for the adopted stopping criterion. The computation of the gradient, $\nabla_\rho \mathcal{G}$, of the compliance with respect to the density has to be provided as well. With this aim, we introduce the Lagrangian functional

$$\mathcal{L} = \mathcal{L}(\mathbf{u}, \mathbf{z}, \rho) = \mathcal{G}(\mathbf{u}) + a_\rho(\mathbf{u}, \mathbf{z}) - \mathcal{G}(\mathbf{z}),$$

where $\mathbf{z} \in U$ is the Lagrange multiplier. It is well known that

$$\nabla_\rho \mathcal{G}(\rho) = \nabla_\rho \mathcal{L}\big|_{\mathbf{u}(\rho),\mathbf{z}(\rho),\rho},$$

where $\mathbf{u}(\rho)$ and $\mathbf{z}(\rho)$ are the solutions to the primal and adjoint problem associated with the Gâteaux derivative of $\mathcal{L}$ with respect to $\mathbf{z}$ and $\mathbf{u}$, respectively. In particular, the primal problem coincides with (9), whereas the adjoint problem is

find $\mathbf{z} \in U$ such that

$$a_\rho(\mathbf{v}, \mathbf{z}) = -\mathcal{G}(\mathbf{v}) \quad \forall \mathbf{v} \in U. \tag{13}$$

On comparing (13) with (9) and due to the self-adjointness of $a_\rho(\cdot,\cdot)$, we infer that $\mathbf{z} = -\mathbf{u}$, that is we have a cost-free adjoint solution. Finally, the Gâteaux derivative of $\mathcal{L}$ with respect to ρ along the direction $\psi \in U$ is

$$\int_\Omega p\, \rho^{p-1} \sigma(\mathbf{u}) : \varepsilon(\mathbf{z}) \psi \, d\Omega = \langle \nabla_\rho \mathcal{G}, \psi \rangle,$$

implying

$$\nabla_\rho \mathcal{G}(\rho) = -p\, \rho^{p-1} \sigma(\mathbf{u}(\rho)) : \varepsilon(\mathbf{u}(\rho)). \tag{14}$$

Thus, each evaluation of the gradient of the compliance requires only a primal solve and the computation of (14).

The output density $\rho_h^{\mathtt{k+1}}$ from `optimize` is then filtered in line 4 by approximating (12) via linear finite elements. The global convergence check in line 5 is based on the difference between two successive iterations of the density with respect to the $L^\infty(\Omega)$-norm.

Other strategies can be adopted as an alternative to Algorithm 2, for example procedures where a more frequent use of the filters inside the optimization routine occurs and/or where $\nabla_\rho \mathcal{G}$ is smoothed as well [59, 60].

3.1 SIMP enriched with anisotropy

To manufacture smooth structures, a sufficiently fine mesh or a heavy density filtering are usually adopted. However, both these choices are often very demanding in terms of computational cost. In [17], the authors propose combining the SIMP procedure with an anisotropic adaptation of the mesh as a computationally efficient alternative. In fact, anisotropic mesh adaptation allows us to reduce the employment of a filter, the optimized structure being intrinsically smooth. This goal is reached by resorting to a rigorous mathematical tool, i.e., an a posteriori error estimator used to generate the anisotropic adapted mesh.

3.1.1 The anisotropic framework

We refer to the setting in [61, 62, 63, 64], where the geometric properties of a generic tetrahedron K are extracted from the spectral properties of the standard

affine transformation T_K, which maps the reference element $\widehat{K}$ inscribed in the unit sphere into K, such that

$$\mathbf{x} = T_K(\hat{\mathbf{x}}) = M_K\hat{\mathbf{x}} + \mathbf{t}_K,$$

with $\mathbf{x} \in K$, $\hat{\mathbf{x}} \in \widehat{K}$, $M_K \in \mathbb{R}^{3\times 3}$, $\mathbf{t}_K \in \mathbb{R}^3$. Through T_K, the unit sphere is transformed into an ellipsoid circumscribing K. By means of the polar decomposition, M_K is factorized as the product $B_K Z_K$, with $B_K \in \mathbb{R}^{3\times 3}$ a symmetric positive definite matrix taking into account the deformation of the element K, and $Z_K \in \mathbb{R}^{3\times 3}$ an orthogonal matrix rigidly rotating K.
Matrix B_K can be decomposed in terms of the corresponding eigenvalues and eigenvectors, leading to $B_K = R_K^T \Lambda_K R_K$, with $R_K^T = [\mathbf{r}_{1,K}, \mathbf{r}_{2,K}, \mathbf{r}_{3,K}]$ and $\Lambda_K = \mathrm{diag}(\lambda_{1,K}, \lambda_{2,K}, \lambda_{3,K})$, with $\lambda_{1,K} \geq \lambda_{2,K} \geq \lambda_{3,K}$. Matrices R_K^T and Λ_K collect all the geometric features of element K. In particular, the eigenvectors $\mathbf{r}_{1,K}$, $\mathbf{r}_{2,K}$ and $\mathbf{r}_{3,K}$ represent the directions of the semi-axes of the ellipsoid circumscribed to K, while the eigenvalues $\lambda_{1,K}$, $\lambda_{2,K}$ and $\lambda_{3,K}$ measure the length of the semi-axes. It is possible to introduce the aspect ratios of the element K,

$$s_{i,K} = \left(\frac{\lambda_{i,K}^2}{\prod_{j\neq i} \lambda_{j,K}} \right)^{2/3}, \quad i = 1, 2, 3,$$

which quantify the anisotropic features of K. Notice that $s_{1,K} \geq s_{2,K} \geq s_{3,K}$ and $s_{1,K}s_{2,K}s_{3,K} = 1$, the isotropic case coinciding with $s_{1,K} = s_{2,K} = s_{3,K} = 1$.

3.1.2 The error estimator

Among the possible a posteriori error estimators available in the literature [65, 66, 67], we resort to a recovery-based analysis [68, 69, 70] which consists of two steps, i.e., the computation of the recovered gradient and the successive definition of the estimator. In [71, 63], an extension of this approach to an anisotropic setting has been proposed for the first time. The recipe adopted for the recovered gradient is

$$P(\nabla u_h)\big|_{\Delta_K} = \frac{1}{|\Delta_K|} \sum_{T\in\Delta_K} |T|\, \nabla u_h|_T,$$

where $\Delta_K = \{T \in \mathcal{T}_h : T \cap K \neq \emptyset\}$ is the patch of elements associated with K. We remark that $P(\nabla u_h)$ is piecewise constant on $\mathcal{T}_h$, differently from the piecewise linear gradient reconstruction adopted in the papers by O.C. Zienkiewicz and J.Z. Zhu. A generalization of $P(\nabla u_h)$ to higher degree reconstructions can be found in [71, 63].

Then, the anisotropic a posteriori error estimator is

$$\eta^2 = \sum_{K\in\mathcal{T}_h} \eta_K^2, \tag{15}$$

where the local contribution η_K is

$$\eta_K^2 = \frac{1}{(\lambda_{1,K}\lambda_{2,K}\lambda_{3,K})^{2/3}} \sum_{i=1}^{3} \lambda_{i,K}^2 \left(\mathbf{r}_{i,K}^T \, G_{\Delta_K}(E_\nabla) \mathbf{r}_{i,K} \right), \tag{16}$$

where $E_\nabla = \left[P(\nabla u_h) - \nabla u_h \right]_{\Delta_K}$ is the recovered error, and $G_{\Delta_K}(\cdot) \in \mathbb{R}^{3\times 3}$ is the symmetric positive semidefinite matrix with entries

$$[G_{\Delta_K}(\mathbf{w})]_{i,j} = \sum_{T\in\Delta_K} \int_T w_i \, w_j \, dT \quad \text{with } i,j = 1,2,3, \tag{17}$$

for any vector-valued function $\mathbf{w} = (w_1, w_2, w_3)^T \in [L^2(\Omega)]^3$. The scaling factor $\left(\lambda_{1,K}\lambda_{2,K}\lambda_{3,K}\right)^{-2/3}$ in (16) ensures the consistency with respect to the isotropic case (i.e., for $\lambda_{1,K} = \lambda_{2,K} = \lambda_{3,K}$).

3.1.3 The SIMPATY algorithm

We resort to a metric-based approach to generate the adapted mesh, by exploting the information contained in η. In more detail, a metric, $\mathcal{M} : \Omega \to \mathbb{R}^{3\times 3}$, is a symmetric positive definite tensor field which contains all the geometric information related to a certain mesh [72]. In a finite element setting, we approximate $\mathcal{M}$ by a piecewise constant function, $\mathcal{M}_{\mathcal{T}_h}$, associated with the actual grid $\mathcal{T}_h$, such that $\mathcal{M}_{\mathcal{T}_h}\big|_K = R_K^T \Lambda_K^{-2} R_K$, consistently with the notation introduced in Section 3.1.1.

We use the local estimator η_K in a predictive way to define a new metric field. This goal is reached via an iterative procedure which, eventually, yields an optimal adapted grid satisfying the two criteria: i) minimization of the number of elements under the accuracy constraint, $\eta \leq \texttt{MTOL}$, with MTOL a user-defined tolerance; ii) error equidistribution, namely, $\eta_K^2 = \texttt{MTOL}^2/\#\mathcal{T}_h$, with $\#\mathcal{T}_h$ the mesh cardinality.

Now, we sketch the procedure adopted for the prediction of the metric out of the estimator, while referring to, e.g., [64, 63] for more details.

With reference to the generic k-th iteration of Algorithm 2, we rewrite estimator η_K by collecting the size information of the patch in a single factor, $|\Delta_K|$, as

$$\eta_K^2 = |\Delta_K| \underbrace{\sum_{i=1}^{3} s_{i,K} \left(\mathbf{r}_{i,K}^T \, \widehat{G}_{\Delta_K}(E_\nabla) \, \mathbf{r}_{i,K} \right)}_{\mathcal{F}(\{s_{i,K}, \mathbf{r}_{i,K}\}_{i=1,2,3})},$$

where $\widehat{G}_{\Delta_K}(\cdot)$ is the scaled matrix $G_{\Delta_K}(\cdot)/|\Delta_K|$, and $|\Delta_K| = \lambda_{1,K}\lambda_{2,K}\lambda_{3,K}\,|\widehat{\Delta}_K|$, with $\widehat{\Delta}_K = T_K^{-1}(\Delta_K)$. Notice that $|\Delta_K|$ is the main quantity related to the volume of the tetrahedra, the other terms keeping track of the orientation and of the stretching of K.

Minimizing the cardinality of the mesh is equivalent to maximizing the size of the patch, so that we are led to solve the constrained minimization problem

$$\min_{s_{i,K},\mathbf{r}_{i,K}} \mathcal{F}(\{s_{i,K},\mathbf{r}_{i,K}\}_{i=1,2,3}) \; : \begin{cases} \mathbf{r}_{i,K}\cdot\mathbf{r}_{j,K} = \delta_{ij} \\ s_{1,K} \geq s_{2,K} \geq s_{3,K} \\ s_{1,K}s_{2,K}s_{3,K} = 1, \end{cases} \tag{18}$$

with δ_{ij} the Kronecker symbol and $i,j = 1,2,3$. This problem has an explicit solution provided in [64, 63] and stated in the following

Proposition 3.1 *Let $\{g_i,\mathbf{g}_i\}_{i=1,2,3}$ be the eigenpairs associated with $\widehat{G}_{\Delta_K}(E_\nabla)$, with $g_1 \geq g_2 \geq g_3 > 0$ and $\{\mathbf{g}_i\}_{i=1,2,3}$ orthonormal. Then, $\mathcal{F}(\cdot)$ is minimized when*

$$s_{1,K} = \frac{\sqrt[3]{\Pi_{i=1}^3 g_i}}{g_3}, \quad s_{2,K} = \frac{\sqrt[3]{\Pi_{i=1}^3 g_i}}{g_2}, \quad s_{3,K} = \frac{\sqrt[3]{\Pi_{i=1}^3 g_i}}{g_1},$$
$$\mathbf{r}_{1,K} = \mathbf{g}_3, \quad \mathbf{r}_{2,K} = \mathbf{g}_2, \quad \mathbf{r}_{3,K} = \mathbf{g}_1.$$

Next, by employing the equidistribution criterion, the optimal values for length $\lambda_{i,K}$ can be computed as

$$\lambda_{1,K} = g_3^{-1/2}\left(\frac{\texttt{MTOL}^2}{3\,\#\mathcal{T}_h|\widehat{\Delta}_K|}\right)^{1/3}\Big(\prod_{i=1}^3 g_i\Big)^{1/18},$$
$$\lambda_{2,K} = g_2^{-1/2}\left(\frac{\texttt{MTOL}^2}{3\,\#\mathcal{T}_h|\widehat{\Delta}_K|}\right)^{1/3}\Big(\prod_{i=1}^3 g_i\Big)^{1/18},$$
$$\lambda_{3,K} = g_1^{-1/2}\left(\frac{\texttt{MTOL}^2}{3\,\#\mathcal{T}_h|\widehat{\Delta}_K|}\right)^{1/3}\Big(\prod_{i=1}^3 g_i\Big)^{1/18}.$$

The optimal piecewise constant metric $\mathcal{M}_{\mathcal{T}_h}$ is thus obtained simply by collecting the optimal values $\{\mathbf{r}_{i,K}\}_{i=1}^3$ and $\{\lambda_{i,K}\}_{i=1}^3$, for each $K \in \mathcal{T}_h$. The optimal metric is finally provided to a metric-based mesh generator to build the adapted mesh. For this task, we employ `mmg3d`, a standalone application suited for grid adaptation [73]. The output file containing the adapted mesh is then read by `FreeFem++`, the environment used to code the whole procedure itemized in Algorithm 3 [17, 18].

Algorithm 3 SIMPATY: SIMP with AdaptiviTY

Input : `CTOL, MTOL, kmax`, $\rho_{\min}$, $\mathcal{T}_h^0$

1: Set: $\rho_h^0 = 1$, $\texttt{k} = 0$, errM = 1+`CTOL`
2: **while** errM > `CTOL` & $\texttt{k} <$ `kmax` **do**
3: $\quad\rho_h^{\texttt{k}+1} = \texttt{optimize}(\rho_h^{\texttt{k}}, \texttt{Mit}, \texttt{TOPT}, \nabla_\rho\mathcal{G}, ...)$;
4: $\quad\mathcal{T}_h^{\texttt{k}+1} = \texttt{adapt}(\mathcal{T}_h^{\texttt{k}}, \rho_h^{\texttt{k}+1}, \texttt{MTOL})$;
5: $\quad\text{errM} = |\#\mathcal{T}_h^{\texttt{k}+1} - \#\mathcal{T}_h^{\texttt{k}}|/\#\mathcal{T}_h^{\texttt{k}}$;
6: $\quad\texttt{k} = \texttt{k} + 1$;

The main difference with respect to Algorithm 2 is in line 4, where mesh adaptation is carried out, with a prescribed tolerance, `MTOL`, on the accuracy. For the stopping criterion, at line 5, we check the stagnation of the adapted meshes through the relative variation of the cardinality of the mesh elements to within `CTOL`.

3.2 Numerical assessment for TO

The same test cases analyzed in Section 2.3 are now tackled by TO.

We remark that `Mit` is usually updated (namely, we decrease `Mit` as `k` increases) within the external loop of Algorithm 3. This choice should allow the optimizer to get very close to the optimal solution on the initial mesh, whereas a less strict check is expected to suffice in the next iterations. Indeed, it is not reasonable to compute an accurate density function on a rough intermediate mesh which is not necessarily the final optimal one.

In order to reduce the computational burden required by TO, we simulate only a quarter of the geometry under investigation, by exploiting the symmetry planes. Precisely, we impose $\mathbf{u} \cdot \mathbf{n} = 0$ on the surfaces where symmetry occurs, and $\mathbf{u} \cdot \mathbf{t} = 0$, with $\mathbf{t}$ the unit tangent vector, on the surfaces where antisymmetry occurs [59]. In Figure 7, the portions of the domain actually employed in the simulations are shown. Once convergence is reached, the complete structures are obtained using reflection tools, avalaible in post processing softwares used for visualization purposes (e.g., Paraview [74]).

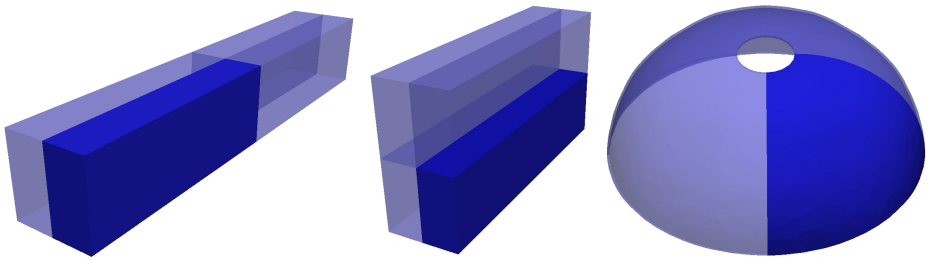

Figure 7: Portion of the domains actually simulated by SIMPATY algorithm.

The input parameters for SIMPATY algorithm are gathered in Table 5. We do not set any value for `TOPT` since we rely only on `Mit` as a stopping criterion for `optimize`.

Test case	`CTOL`	`MTOL`	`kmax`	$\rho_{\min}$
Bridge	1e-2	0.35	10	0.001
Cantilever beam	5e-3	0.09	10	0.001
Dome	5e-3	1.10	7	0.001

Table 5: Input data to SIMPATY algorithm.

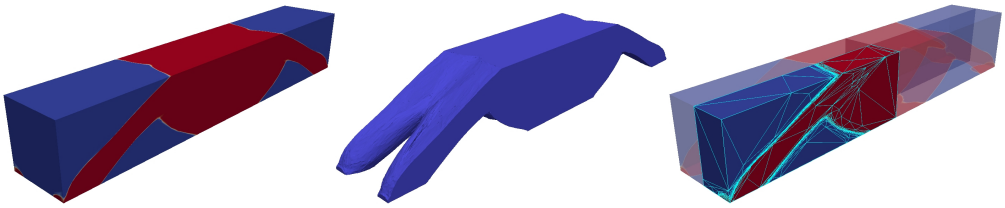

Figure 8: The bridge test case (TO): density field (left), final structure (center), and a quarter of the domain with both density and adapted mesh (right) as delivered by SIMPATY.

3.2.1 The bridge test case

The topology optimization of the bridge is carried out with SIMPATY by setting a volume fraction $\alpha = 0.4$, `Mit` $= 100$ for the first iteration, 50 for the second, and 25 for the subsequent ones, and selecting an initial mesh of 52556 elements.

The resulting function ρ in Figure 8, left is characterized by a sharp alternation of void and full material and by very thin layers. The corresponding structure (Figure 8, center), obtained by a truncation procedure which keeps only the elements of the mesh where $\rho|_K \geq 0.5$, exhibits very smooth boundaries and it is almost ready for the printing process. Figure 8, right, shows the domain actually employed in the simulations, with the final adapted mesh superposed to the density. In particular, the adapted mesh sharply detects the void/material interface with very stretched tetrahedra. This is more evident in Figure 9, which focuses on the external faces from three different view angles. The elements are highly stretched along the boundaries of the structure and they massively concentrate in these portions of the domain. Instead, where the design variable is smooth, the mesh is coarse, reducing the computational burden of the simulation.

The resulting structure, seen from different angles, is shown in Figure 10. We can appreciate the smoothness of the boundary surfaces, which is made possible by the optimal shape, size and orientation of the mesh elements. In particular, from the bottom view, some complex features of the structure are evident, as further highligthed in the slice-plot shown in Figure 11.

In Table 6, some quantitative results are provided. As expected, the mass reduction is responsible for a slight increase of the compliance.

$\mathcal{G}$ before TO	0.0933	[J]
$\mathcal{G}$ after TO	0.1009	[J]
$\Delta_{\%}\mathcal{G}$	+8.15%	[-]
$\#\mathcal{T}_h$	95482	[-]

Table 6: The bridge test case (TO): compliance before and after TO, percentage variation of the compliance, cardinality of the final adapted mesh.

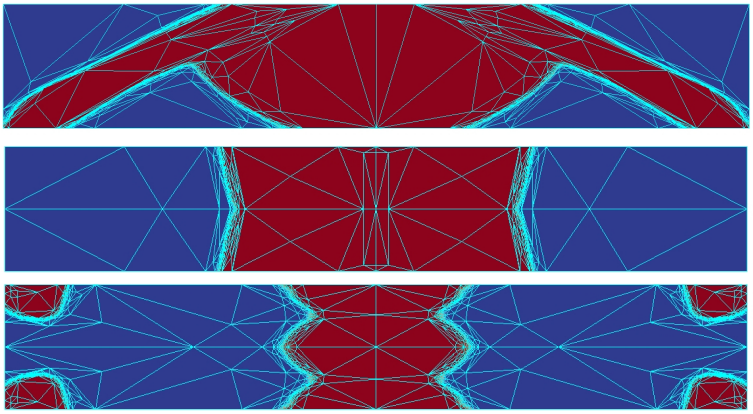

Figure 9: The bridge test case (TO): frontal (top), top (center), and bottom (bottom) views of the density superposed to the adapted mesh.

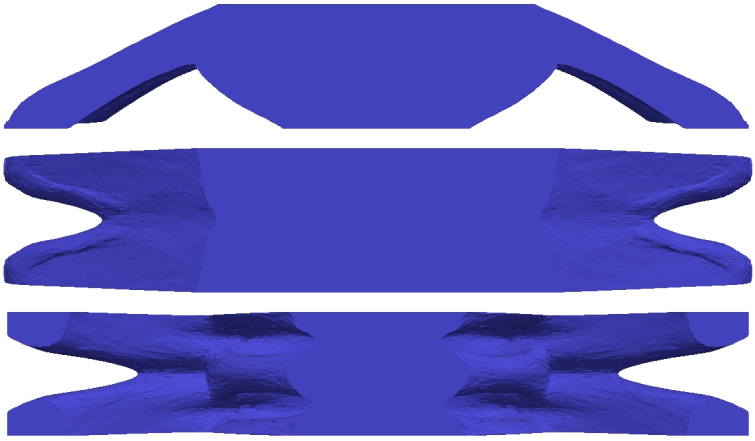

Figure 10: The bridge test case (TO): frontal (top), top (center), and bottom (bottom) views of the structure returned by SIMPATY.

3.2.2 The cantilever test case

Results for the topology optimized cantilever beam are shown in Figure 12. We pick $\alpha = 0.5$, `Mit` $= 75$ for the first iteration, 50 for the following ones, and $\mathcal{T}_h^0$ a uniform mesh consisting of 35280 tetrahedra.

The final structure is very smooth (see Figures 12-14). Despite the apparent massive external shell, an internal cavity is generated by SIMPATY to lighten the optimized structure as it is also evident from the slice plot in Figure 15. The anisotropic features of the adapted mesh are able to sharply capture the interface between material and void, considerably coarsening the mesh in the areas inside and outside the structure.

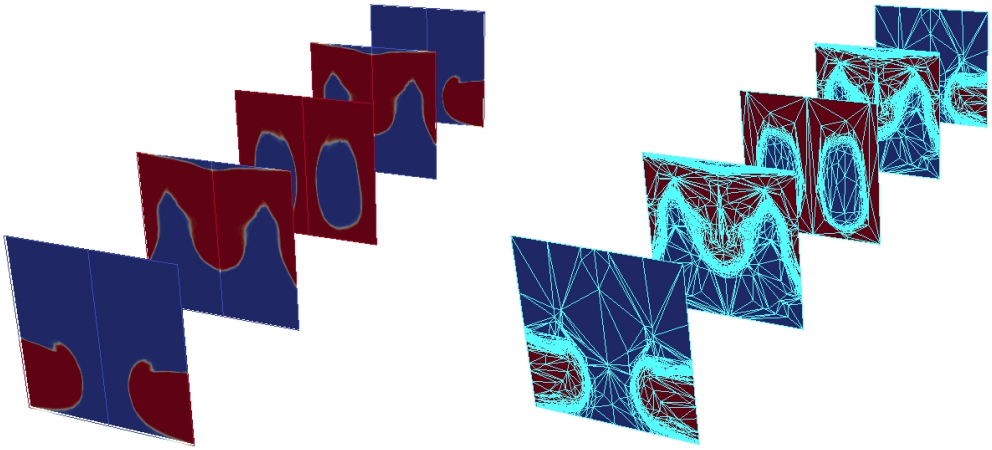

Figure 11: The bridge test case (TO): slices of the density (left) and of the adapted mesh (right).

Concerning the quantitative data in Table 7, we have that the reduction of half the mass of the cantilever leads to a considerable increment of the compliance, which almost triplicates with respect to the initial value. Despite the contained number of tetrahedra, the final structure generated by SIMPATY is almost ready to print with a reasonable mechanical response.

$\mathcal{G}$ before TO	0.0309	[J]
$\mathcal{G}$ after TO	0.0867	[J]
$\Delta_{\%}\mathcal{G}$	180%	[-]
$\#\mathcal{T}_h$	96038	[-]

Table 7: The cantilever test case (TO): compliance before and after TO, percentage variation of the compliance, cardinality of the final adapted mesh.

3.2.3 The dome test case

For the dome test case, we set $\alpha = 0.2$, `Mit` $= 120$ for the first iteration, 60 for the second, and 20 for the subsequent ones, and we employ an initial grid of 20857 elements.

The final layout for the optimized dome is shown in Figure 16, where the smooth final density, left is shown along with a close-up of the quarter of domain actually employed, right. In addition, three views of the obtained structure are provided in Figure 17. SIMPATY algorithm turns out to be effective also in the case of a thin shell domain. In some way, the obtained layout can be identified with a macro-grid, in the spirit of a Michell structure [75]. Finally, Figure 18 shows how the anisotropic mesh closely follows the distribution of the material

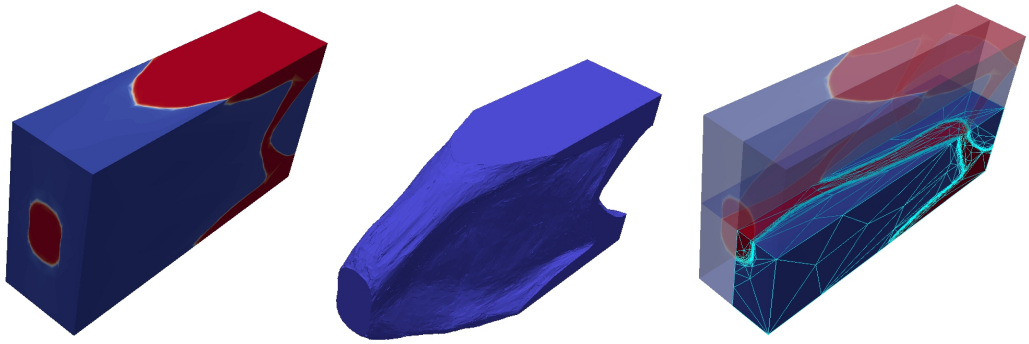

Figure 12: The cantilever test case (TO): density field (left), final structure (center), and a quarter of the domain with both density and adapted mesh (right) as delivered by SIMPATY.

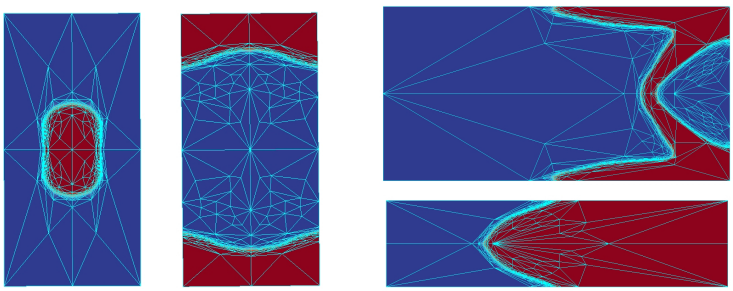

Figure 13: The cantilever test case (TO): frontal (top), rear (center), lateral (right-top), and top (right-bottom) views of the density superposed to the adapted mesh.

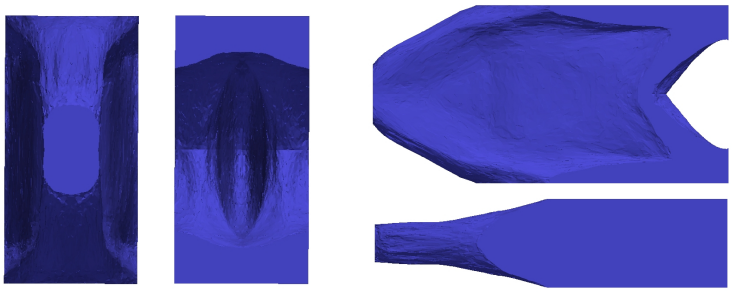

Figure 14: The cantilever test case (TO): frontal (left), rear (center), lateral (right-top), and top (right-bottom) views of the structure returned by SIMPATY.

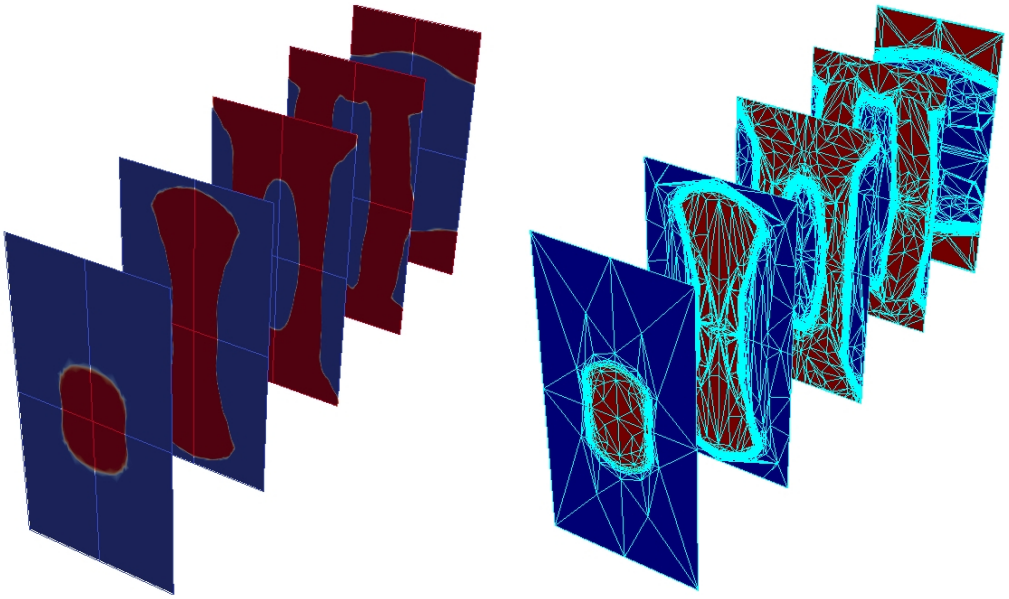

Figure 15: The cantilever test case (TO): slices of the density (left) and of the adapted mesh (right).

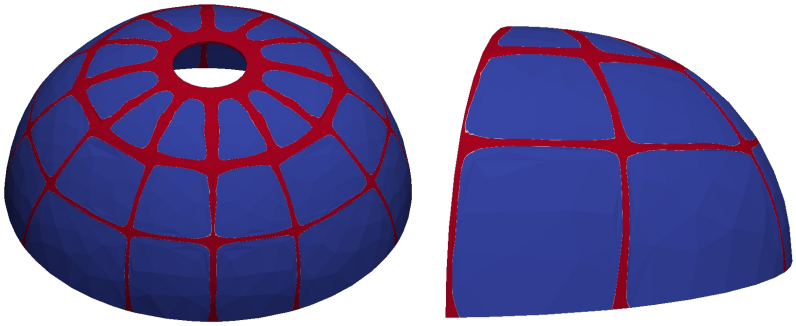

Figure 16: The dome test case (TO): density (left), and a quarter of the domain close-up (right) as delivered by SIMPATY.

despite the very thready components of the optimized dome.

The values collected in Table 8 show that a considerable reduction of the mass of the final configuration leads to a slight increase in the compliance. The number of elements in the final configuration is rather high likely due to the curvature of the geometry. The software `mmg3d` includes options to control the geometric features of the domain, so that the mesh can follow the original curvature of the surface to within a threshold.

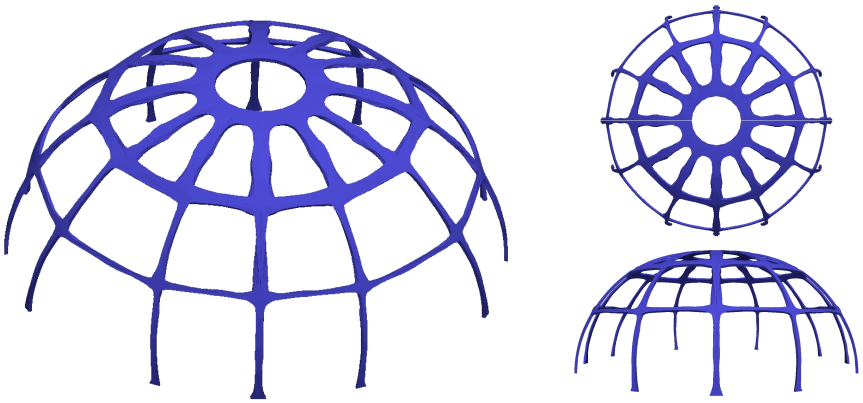

Figure 17: The dome test case (TO): frontal (left), top (right-top), and lateral (right-bottom) views of the structure returned by SIMPATY.

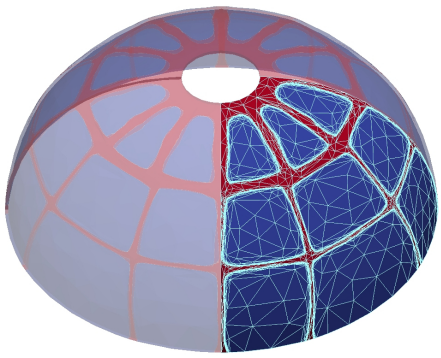

Figure 18: The dome test case (TO): adapted mesh superposed to the density for a quarter of the domain.

$\mathcal{G}$ before TO	7.1654	[J]
$\mathcal{G}$ after TO	7.7265	[J]
$\Delta_{\%}\mathcal{G}$	+7.83%	[-]
$\#\mathcal{T}_h$	118435	[-]

Table 8: The dome test case (TO): compliance before and after TO, percentage variation of the compliance, cardinality of the final adapted mesh.

3.2.4 A comparison with another approach in the literature.

We compare the performance of SIMPATY algorithm with the anisotropic mesh adaptation proposed in [59]. The main difference in the two algorithms lies in the driving force for the adaptation procedure, namely an actual error estimator in SIMPATY versus a heuristic indicator based on the filtered Hessian of the

density and of a filtered sensitivity. In contrast, we essentially do not apply any filtering.

In particular, we consider the same configuration as in Figure 9 of [59]. The structure provided by SIMPATY (see Figure 19) is topologically comparable with the one in [59].

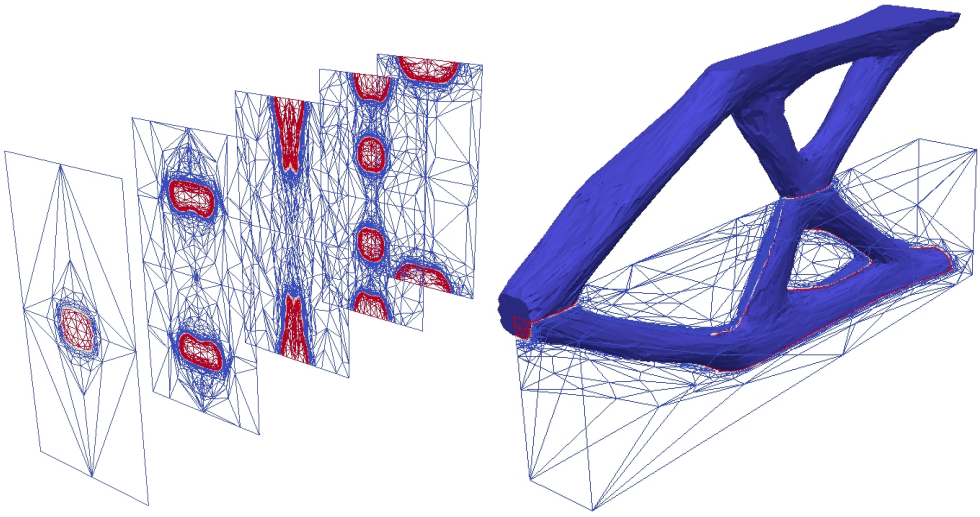

Figure 19: Comparison with [59]: slice plot for the density and the adapted mesh (top); whole optimized structure and adapted mesh on the simulated quarter of domain (bottom).

From a quantitative viewpoint, the outcome from SIMPATY provides a slightly better performing structure, characterized by a compliance equal to 1.2996 versus a compliance of 1.5529 in [59]. Moreover, SIMPATY converges in 9 iterations after 0.76 [h][1], providing a final mesh with 4205 nodes to be compared with 3.3 [h] and 3121 vertices in [59].

4 The coupling of shape and topology optimization

So far, shape and topology optimization have been applied separately. The goal now is to combine them in order to improve the overall performance of the optimization (see, e.g., [19, 20, 21, 22, 23]).

On the one hand, TO delivers light structures with a mass reduction with respect to the initial configuration but with a higher compliance. On the other hand, SO ensures a reduction of the compliance keeping the volume fixed. Hence, the idea here is to sequentially couple the two techniques to take advantage of the benefits of both of them.

[1]The computations have been run on a GenuineIntel Pentium(R) Dual-Core CPU E6300 2.80 GHz 4GB RAM desktop computer.

In principle, there are at least three possibile combinations of topology and shape optimization: SO first and TO after (STO), TO first and SO after (TSO), and SO and TO iteratively intertwined. We pursue the first approach, namely, we first move *out of the box* the boundary of the design domain by means of SO. Then, the resulting structure is topologically optimized by means of the SIMPATY algorithm. The choice for STO instead of TSO is justified by the observation that the shape optimization of an already topologically optimized structure emphasizes the thinning of the thready components, even leading to invalid mesh elements, and, in general, to non-manufacturable layouts. These drawbacks may be amplified by a more tight alternation between SO and TO, while are generally mitigated by a STO approach.

The STO procedure is listed in Algorithm 4.

Algorithm 4 Shape and Topology Optimization (STO)

Input : `CTOL, MTOL, ktmax, ksmax`, Δ_{BEST}, $\mathcal{T}_h^0$, V_0, $\rho_{\min}$

Set: $\mathtt{ks} = 0$, $\mathtt{k}_{BEST} = 0$, $\mathcal{T}_{BEST} = \mathcal{T}_h^0$, $\mathcal{G}_{BEST} = \mathcal{G}(\Omega^0)$;
while $\mathtt{ks} - \mathtt{k}_{BEST} < \Delta_{BEST}$ & $\mathtt{ks} < \mathtt{ksmax}$ **do**
    Solve (6);
    Solve (7);
    Compute $\phi^{\mathtt{k}}$, $\ell^{\mathtt{k}}$;
    $\mathcal{T}_h^{\mathtt{ks}+1} = \mathtt{movemesh}(\mathcal{T}_h^{\mathtt{ks}}, \mathbf{d}_h^{\mathtt{ks}}, \ell^{\mathtt{ks}})$;
    while $\mathcal{T}_h^{\mathtt{ks}+1}$ has degenerate elements **do**
        Reduce $\ell^{\mathtt{ks}}$;
        $\mathcal{T}_h^{\mathtt{ks}+1} = \mathtt{movemesh}(\mathcal{T}_h^{\mathtt{ks}}, \mathbf{d}_h^{\mathtt{ks}}, \ell^{\mathtt{ks}})$;
    $\mathcal{T}_h^{\mathtt{ks}+1} = \mathtt{regularize}\ (\mathcal{T}_h^{\mathtt{ks}+1})$;
    Compute $\mathcal{G}(\Omega)$;
    if $\mathcal{G}(\Omega) < \mathcal{G}_{BEST}$ **then**
        $\mathcal{G}_{BEST} = \mathcal{G}(\Omega)$;
        $\mathtt{k}_{BEST} = \mathtt{ks} + 1$;
        $\mathcal{T}_{BEST} = \mathcal{T}_h^{\mathtt{ks}+1}$;
    $\mathtt{ks} = \mathtt{ks} + 1$;
Set: $\rho_h^0 = 1$, $\mathtt{kt} = 0$, errM $= 1 +$ `CTOL`, $\mathcal{T}_h^0 = \mathcal{T}_h^{\mathtt{ks}}$
while errM $>$ `CTOL` & $\mathtt{kt} < \mathtt{ktmax}$ **do**
    $\rho_h^{\mathtt{kt}+1} = \mathtt{optimize}\ (\rho_h^{\mathtt{kt}}, \mathtt{Mit}, \mathtt{TOPT}, \nabla_\rho \mathcal{G}, ...)$;
    $\mathcal{T}_h^{\mathtt{kt}+1} = \mathtt{adapt}(\mathcal{T}_h^{\mathtt{kt}}, \rho_h^{\mathtt{kt}+1}, \mathtt{MTOL})$;
    errM $= |\#\mathcal{T}_h^{\mathtt{kt}+1} - \#\mathcal{T}_h^{\mathtt{kt}}|/\#\mathcal{T}_h^{\mathtt{kt}}$;
    $\mathtt{kt} = \mathtt{kt} + 1$;

4.1 Numerical assessment for STO

We re-run the test cases analyzed for SO and TO. The parameters for SO are the same as those in Section 2.3. Instead, the values for TO are listed in Table 9,

the volume fraction α being the same as in Section 3.2.

Test case	`CTOL`	`MTOL`	`ktmax`	$\rho_{\min}$
Bridge	5e-3	0.01	15	0.001
Cantilever	1e-3	0.075	10	0.001
Dome	5e-3	1.00	11	0.001

Table 9: Input data to SIMPATY algorithm for STO.

4.1.1 The bridge test case

The STO bridge is shown in Figures 20-23. It is evident the combined effect of SO with TO. In particular, we recognize as external shape the one delivered by the single SO (compare with Figure 2), whereas the two spans of the bridge are yielded by TO similarly to what obtained in Figure 8, center. Notice that the final structure is sufficiently symmetric, even though no symmetry condition is enforced in the algorithm. This can be ascribed to the sufficiently fine isotropic grid used as initial mesh $\mathcal{T}_h^0$, consisting of 10477 tetrahedra, so that the results are not biased by a poor discretization.

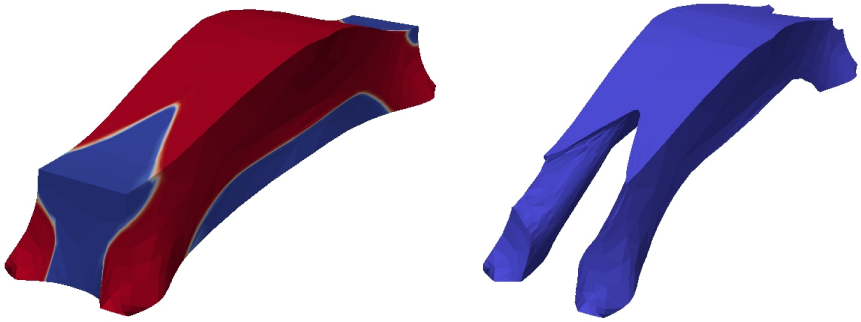

Figure 20: The bridge test case (STO): density field (left) and final structure (right).

Finally, Table 10 highlights the reduction of the objective function with respect to the non-optimized case. The benefits due to SO in terms of structure stiffness are not thoroughly compromised by the TO step. Additionally, the number of elements in the final mesh is considerably low for a full 3D simulation.

4.1.2 The cantilever test case

The cantilever beam yielded by Algorithm 4 starting from an initial mesh comprising 120355 elements, is displayed in Figures 24-26. The external shape is essentially the same as in Figure 4, while the inner topology has considerably

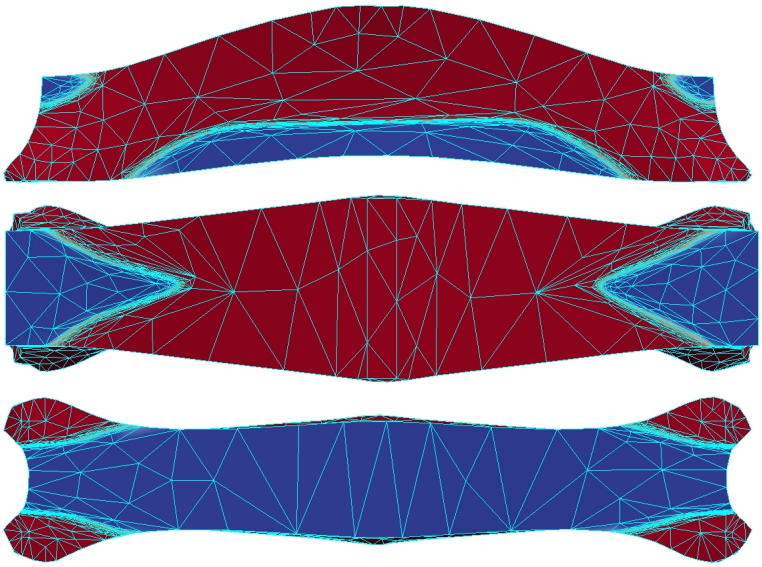

Figure 21: The bridge test case (STO): frontal (top), top (center), and bottom (bottom) views of the density superposed to the adapted mesh.

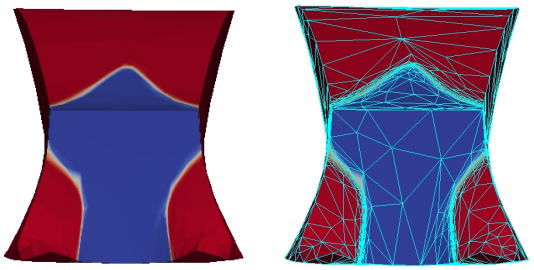

Figure 22: The bridge test case (STO): lateral view of the density (left) and of the density superposed to the adapted mesh (right).

$\mathcal{G}$ before STO	0.0933	[J]
$\mathcal{G}$ after STO	0.0820	[J]
$\Delta_{\%}\mathcal{G}$	-12.12%	[-]
$\#\mathcal{T}_h$	40301	[-]

Table 10: The bridge test case (STO): compliance before and after STO, percentage variation of the compliance, cardinality of the final adapted mesh.

changed with respect to that provided by the sole SIMPATY algorithm. Indeed, we recognize the presence of an additional cavity in the frontal part of the cantilever, as clearly highlighted by comparing Figure 14 with Figure 26. This

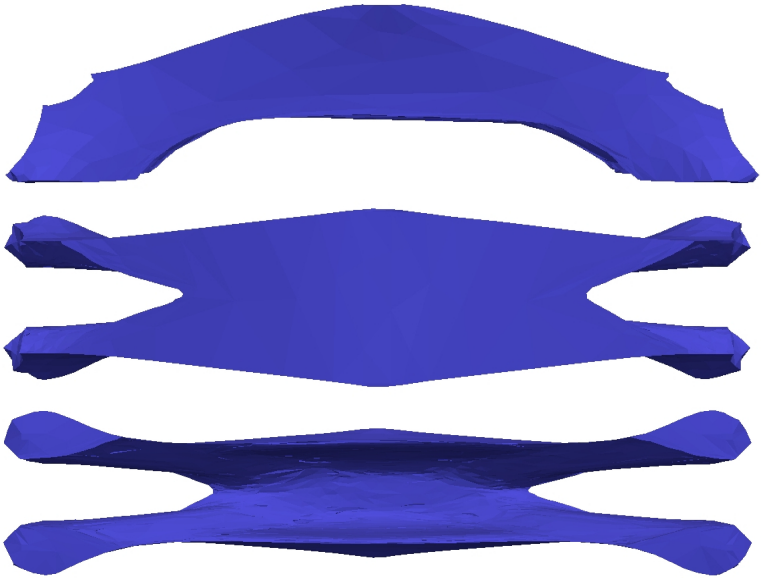

Figure 23: The bridge test case (STO): frontal (top), top (center), and bottom (bottom) views of the final structure.

redistribution of the material makes the structure stiffer in the STO case with respect to the TO case, as confirmed by the values in Tables 7 and 11. A slight lack of symmetry can be observed in the final configuration.

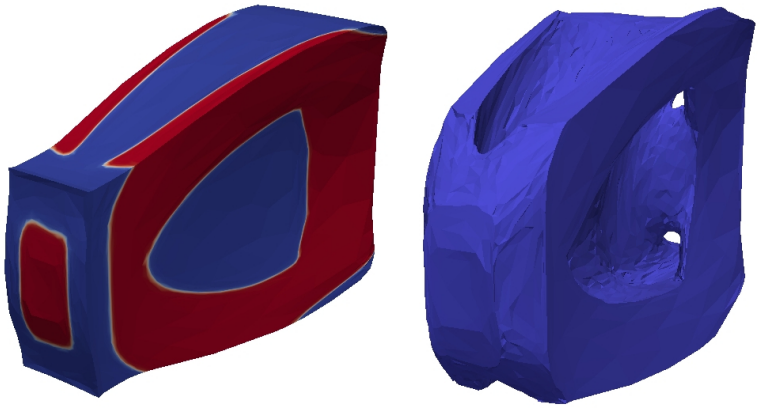

Figure 24: The cantilever test case (STO): density field (left) and final structure (right).

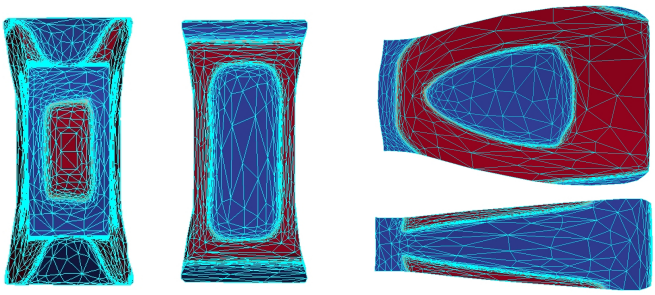

Figure 25: The cantilever test case (STO): frontal (left), rear (middle), lateral (right-top), and top (right-bottom) views of the density superposed to the adapted mesh.

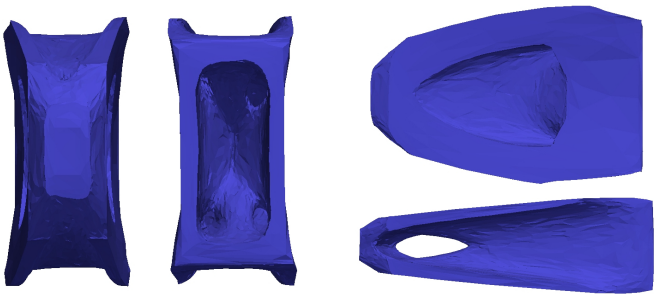

Figure 26: The cantilever test case (STO): frontal (left), rear (middle), lateral (right-top), and top (right-bottom) views of the final structure.

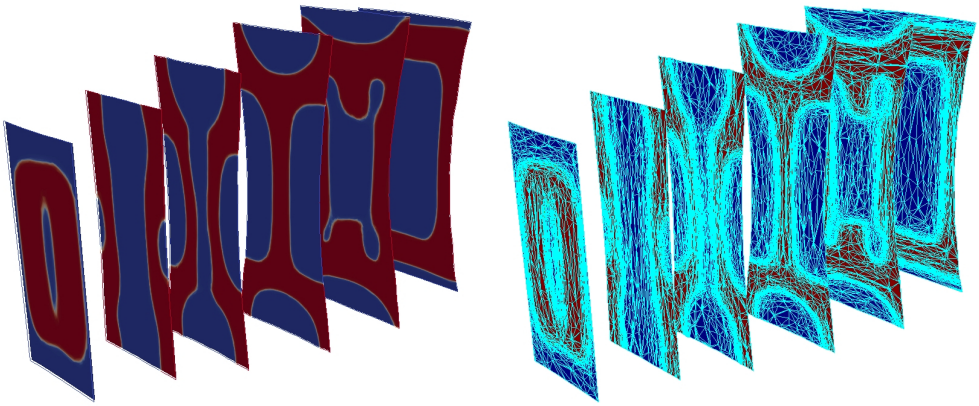

Figure 27: The cantilever test case (STO): slices of the density (left) and of the adapted mesh (right).

$\mathcal{G}$ before STO	0.0309	[J]
$\mathcal{G}$ after STO	0.0162	[J]
$\Delta_{\%}\mathcal{G}$	-47.4%	[-]
$\#\mathcal{T}_h$	127513	[-]

Table 11: The cantilever test case (STO): compliance before and after STO, percentage variation of the compliance, cardinality of the final adapted mesh.

4.1.3 The dome test case

The structure obtained for the dome geometry initially tiled by 92964 elements, is completely different from a straightforward merging of the effects of SO and TO. A two-story layout for STO replaces the three-story configuration in Figure 17. Additionally, we loose the radial symmetry of the TO case.

Finally, the values in Table 12 confirm the trend of the other test cases, with a net decrease of the compliance despite the drastic reduction of the total mass by 80%.

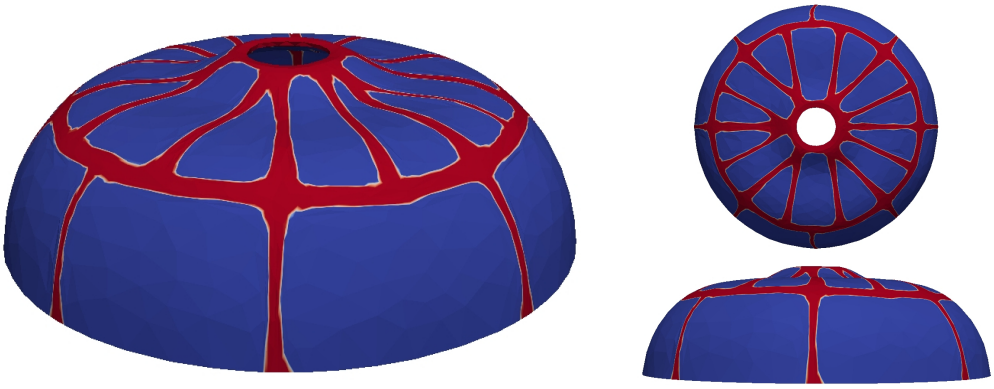

Figure 28: The dome test case (STO): frontal (left), top (right-top), and lateral (right-bottom) views of the final density field.

$\mathcal{G}$ before STO	7.1654	[J]
$\mathcal{G}$ after STO	6.9127	[J]
$\Delta_{\%}\mathcal{G}$	-3.52%	[-]
$\#\mathcal{T}_h$	37143	[-]

Table 12: The dome test case (STO): compliance before and after STO, percentage variation of the compliance, cardinality of the final adapted mesh.

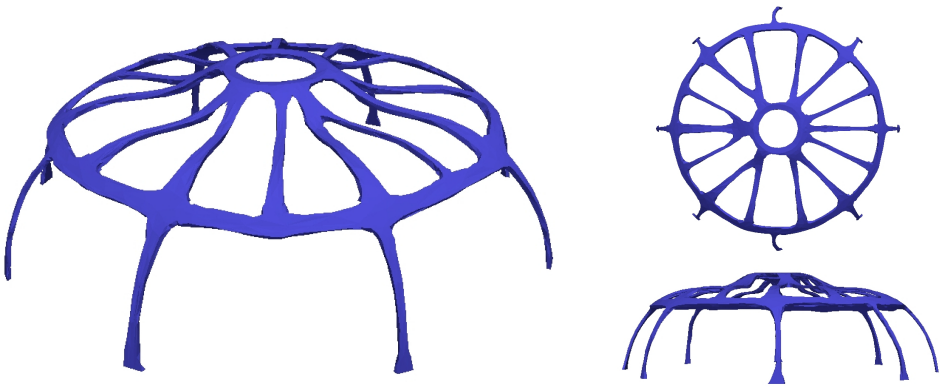

Figure 29: The dome test case (STO): frontal (left), top (right-top), and lateral (right-bottom) views of the final structure.

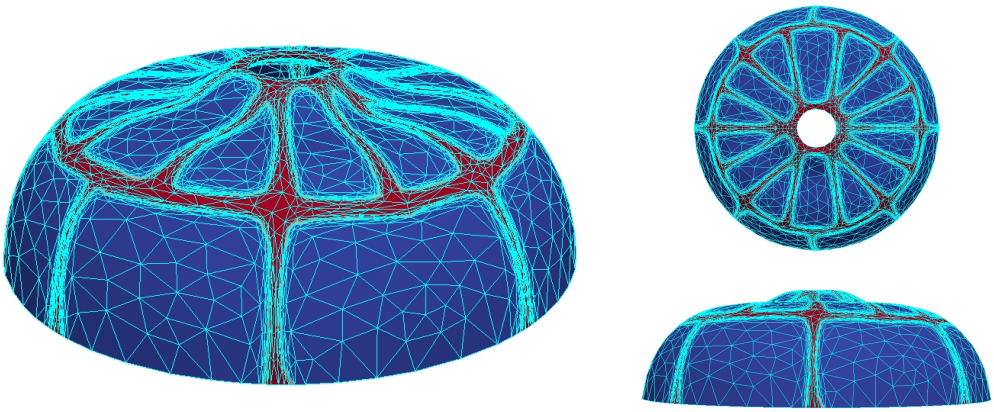

Figure 30: The dome test case (STO): frontal (left), top (right-top), and lateral (right-bottom) views of adapted mesh superposed to the density.

5 Conclusions and future developments

We proposed a new technique for structure design, combining shape optimization (SO) with topology optimization (TO) in order to minimize the compliance of the final layout. A sequential coupling of these two procedures is here enriched by the added value of anisotropic mesh adaptation. The merging between SO and TO allows us to take advantage of the benefits of each single technique. In particular, shape optimization moves the optimized structure out of the initial design domain with a reduction in terms of compliance. Successively, topology optimization is applied to reduce the total mass in the final structure with an increment of the compliance. The main advantage of the sequential coupling is that the increase of the compliance due to the TO step in the STO procedure is

not sufficient to compromise the compliance reduction provided by the SO phase, thus ensuring a final benefit in terms of mechanical performance (see Table 13).

The introduction of an anisotropic mesh adaptation procedure has proven to be a key feature. In particular, it allows us to obtain very smooth structures, essentially ready to print, thus avoiding any post-processing.

Test case	Initial $\mathcal{G}$	$\mathcal{G}$ after SO	$\Delta_{\%}\mathcal{G}$	$\mathcal{G}$ after TO	$\Delta_{\%}\mathcal{G}$	$\mathcal{G}$ after STO	$\Delta_{\%}\mathcal{G}$
Bridge	0.0933 [J]	0.0796 [J]	-14.68%	0.1009 [J]	+8.15%	0.0820 [J]	-12.12%
Cantilever	0.0309 [J]	0.0104 [J]	-66.34%	0.0867 [J]	+180%	0.0162 [J]	-47.4%
Dome	7.1654 [J]	3.2433 [J]	-54.74%	7.7265 [J]	+7.83%	6.9127 [J]	-3.52%

Table 13: Compliance before and after SO, TO and STO and corresponding percentage variation of the compliance for the three test cases.

Possible future developments of this research include the validation of the STO algorithm on more realistic configurations and the generalization of the procedure to a multi-objective context.

Acknowledgments

The authors acknowledge Tommaso Ferri who carried out the first numerical assessments in [76] under the supervision of the last two authors. Furthermore, we acknowledge the research project GNCS-INdAM 2018 “Tecniche di Riduzione di Modello per le Applicazioni Mediche”, which partially supported this research.

References

[1] G. Allaire, G. A. Francfort, A numerical algorithm for topology and shape optimization, in: Topology design of structures (Sesimbra, 1992), Vol. 227 of NATO Adv. Sci. Inst. Ser. E Appl. Sci., Kluwer Acad. Publ., Dordrecht, 1993, pp. 239–248.

[2] N. V. Banichuk, Introduction to Optimization of Structures, Springer-Verlag, New York, 1990.

[3] M. P. Bendsøe, O. Sigmund, Topology Optimization, Springer-Verlag, Berlin, 2003.

[4] Z. D. Ma, N. Kikuchi, I. Higiwara, Structural topology and shape optimization for a frequency response problem, Comput. Mech. 13 (3) (1993) 157–174.

[5] U. Kirsch, Optimum Structural Design: Concepts, Methods, and Applications, McGraw-Hill, 1991.

[6] O. Sigmund, K. Maute, Topology optimization approaches, Struct. Multidiscip. Optim. 48 (6) (2013) 1031–1055.

[7] O. Pironneau, Optimal Shape Design for Elliptic Systems, Springer Series in Computational Physics, Springer-Verlag, New York, 1984.

[8] J. Sokolowski, J.-P. Zolésio, Introduction to shape optimization, in: Introduction to Shape Optimization: Shape Sensitivity Analysis, Springer Berlin Heidelberg, Berlin, Heidelberg, 1992, pp. 5–12.

[9] G. I. N. Rozvany, A critical review of established methods of structural topology optimization, Struct. Multidiscip. Optim. 37 (2009) 217–237.

[10] J.-P. Zolésio, Introduction to shape optimization problems and free boundary problems, in: Shape Optimization and Free Boundaries (Montreal, PQ, 1990), Vol. 380 of NATO Adv. Sci. Inst. Ser. C Math. Phys. Sci., Kluwer Acad. Publ., Dordrecht, 1992, pp. 397–457.

[11] C. Woodward, Methods for computer-aided design of free-form objects, Acta Polytech. Scand. Math. Comput. Sci. Ser. (56) (1990) 60.

[12] S. Cai, W. Zhang, Stress constrained topology optimization with free-form design domains, Comput. Methods Appl. Mech. Engrg. 289 (2015) 267–290.

[13] G. Allaire, R. V. Kohn, Optimal design for minimum weight and compliance in plane stress using extremal microstructures, European J. Mech. A Solids 12 (6) (1993) 839–878.

[14] S. I. Valdez, S. Botello, M. A. Ochoa, J. L. Marroquín, V. Cardoso, Topology optimization benchmarks in 2D: results for minimum compliance and minimum volume in planar stress problems, Arch. Comput. Methods Eng. 24 (4) (2017) 803–839.

[15] J. Wu, A. Clausen, O. Sigmund, Minimum compliance topology optimization of shell-infill composites for additive manufacturing, Comput. Methods Appl. Mech. Engrg. 326 (2017) 358–375.

[16] P. L. Gould, Introduction to Linear Elasticity, Springer–Verlag, New York, 1994.

[17] S. Micheletti, S. Perotto, L. Soli, Topology optimization driven by anisotropic mesh adaptation: towards free-form design, submitted.

[18] S. Micheletti, S. Perotto, L. Soli, Ottimizzazione topologica adattativa per la fabbricazione stratificata additiva, Italian patent application No. 102016000118131, filed on November 22, 2016 (extended as *Adaptive topology optimization for additive layer manufacturing*, International patent application PCT No. PCT/IB2017/057323) (2017).

[19] O. Pantz, K. Trabelsi, Simultaneous shape, topology, and homogenized properties optimization, Struct. Multidiscip. Optim. 34 (4) (2007) 361–365.

[20] N. Jenkins, K. Maute, An immersed boundary approach for shape and topology optimization of stationary fluid-structure interaction problems, Struct. Multidiscip. Optim. 54 (5) (2016) 1191–1208.

[21] Y. Wang, Z. Kang, A level set method for shape and topology optimization of coated structures, Comput. Methods Appl. Mech. Engrg. 329 (2018) 553–574.

[22] C. Dapogny, A. Faure, G. Michailidis, G. Allaire, A. Couvelas, R. Estevez, Geometric constraints for shape and topology optimization in architectural design, Comput. Mech. 59 (6) (2017) 933–965.

[23] F. de Gournay, G. Allaire, F. Jouve, Shape and topology optimization of the robust compliance via the level set method, ESAIM Control Optim. Calc. Var. 14 (1) (2008) 43–70.

[24] P. W. Christensen, A. Klarbring, An Introduction to Structural Optimization, Vol. 153 of Solid Mechanics and its Applications, Springer, New York, 2009.

[25] A. Paganini, F. Wechsung, P. E. Farrell, Higher-order moving mesh methods for PDE-constrained shape optimization, SIAM J. Sci. Comput. 40 (4) (2018) A2356–A2382.

[26] E. K. Chong, S. H. Zak, An Introduction to Optimization, Vol. 76, John Wiley & Sons, 2013.

[27] J. Nocedal, S. J. Wright, Numerical Optimization, Springer Series in Operations Research, Springer-Verlag, New York, 1999.

[28] H. Harbrecht, Analytical and numerical methods in shape optimization, Math. Methods Appl. Sci. 31 (18) (2008) 2095–2114.

[29] G. Allaire, C. Dapogny, P. Frey, Shape optimization with a level set based mesh evolution method, Comput. Methods Appl. Mech. Engrg. 282 (2014) 22–53.

[30] G. Allaire, O. Pantz, Structural optimization with FreeFem++, Struct. Multidiscip. Optim. 32 (3) (2006) 173–181.

[31] G. Allaire, F. Jouve, A.-M. Toader, Structural optimization using sensitivity analysis and a level-set method, J. Comput. Phys. 194 (1) (2004) 363–393.

[32] P. G. Ciarlet, The Finite Element Method for Elliptic Problems, North-Holland Publishing Co., Amsterdam-New York-Oxford, 1978.

[33] G. Allaire, F. de Gournay, F. Jouve, A.-M. Toader, Structural optimization using topological and shape sensitivity via a level set method, Control Cybernet. 34 (1) (2005) 59–80.

[34] F. Hecht, New development in FreeFem++, J. Numer. Math. 20 (3-4) (2012) 251–265.

[35] S. Amstutz, Connections between topological sensitivity analysis and material interpolation schemes in topology optimization, Struct. Multidiscip. Optim. 43 (6) (2011) 755–765.

[36] M. P. Bendsøe, O. Sigmund, Material interpolation schemes in topology optimization, Arch. Appl. Mech. 69 (9) (1999) 635–654.

[37] M. P. Bendsøe, Optimal shape design as a material distribution problem, Struct. Optimization 1 (4) (1989) 193–202.

[38] M. P. Bendsøe, Optimization of Structural Topology, Shape, and Material, Springer-Verlag, Berlin, 1995.

[39] M. Y. Wang, X. Wang, D. Guo, A level set method for structural topology optimization, Comput. Methods Appl. Mech. Engrg. 192 (1-2) (2003) 227–246.

[40] M. Burger, S. J. Osher, A survey on level set methods for inverse problems and optimal design, European J. Appl. Math. 16 (2) (2005) 263–301.

[41] V. J. Challis, J. K. Guest, Level set topology optimization of fluids in Stokes flow, Int. J. Numer. Meth. Engng 79 (10) (2009) 1284–1308.

[42] G. Allaire, Shape Optimization by the Homogenization Method, Vol. 146 of Applied Mathematical Sciences, Springer-Verlag, New York, 2002.

[43] M. P. Bendsøe, N. Kikuchi, Generating optimal topologies in structural design using a homogenization method, Comput. Methods Appl. Mech. Engrg. 71 (2) (1988) 197–224.

[44] A. R. Díaz, M. P. Bendsøe, Shape optimization of structures for multiple loading conditions using a homogenization method, Struct. Optim. 4 (1) (1992) 17–22.

[45] B. Bourdin, A. Chambolle, Design-dependent loads in topology optimization, ESAIM Control Optim. Calc. Var. 9 (2003) 19–48.

[46] H. Garcke, C. Hecht, M. Hinze, C. Kahle, Numerical approximation of phase field based shape and topology optimization for fluids, SIAM J. Sci. Comput. 37 (4) (2015) A1846–A1871.

[47] L. Dedè, M. J. Borden, T. J. R. Hughes, Isogeometric analysis for topology optimization with a phase field model, Arch. Comput. Methods Eng. 19 (3) (2012) 427–465.

[48] O. Sigmund, On the usefulness of non-gradient approaches in topology optimization, Struct. Multidiscip. Optim. 43 (5) (2011) 589–596.

[49] D. J. Munk, G. A. Vio, G. P. Steven, Topology and shape optimization methods using evolutionary algorithms: a review, Struct. Multidiscip. Optim. 52 (3) (2015) 613–631.

[50] O. Sigmund, J. Petersson, Numerical instabilities in topology optimization: a survey on procedures dealing with checkerboards, mesh-dependencies and local minima, Struct. Optim. 16 (1) (1998) 68–75.

[51] A. A. Gomes, A. Suleman, Application of spectral level set methodology in topology optimization, Struct. Multidiscip. Optim. 31 (6) (2006) 430–443.

[52] C. H. Villanueva, K. Maute, CutFEM topology optimization of 3D laminar incompressible flow problems, Comput. Methods Appl. Mech. Engrg. 320 (2017) 444–473.

[53] M. Giacomini, O. Pantz, K. Trabelsi, Volumetric expressions of the shape gradient of the compliance in structural shape optimization, arXiv:1701.05762 (2017).

[54] A. Díaz, O. Sigmund, Checkerboard patterns in layout optimization, Struct. Multidiscip. Optim. 19 (1995) 89–92.

[55] B. S. Lazarov, O. Sigmund, Filters in topology optimization based on Helmholtz-type differential equations, Int. J. Numer. Meth. Engng 86 (6) (2011) 765–781.

[56] A. Wächter, L. T. Biegler, On the implementation of an interior-point filter line-search algorithm for large-scale nonlinear programming, Math. Program. 106 (1, Ser. A) (2006) 25–57.

[57] K. Svanberg, The method of moving asymptotes-a new method for structural optimization, Int. J. Numer. Meth. Engng 24 (2) (1987) 359–373.

[58] A. Wächter, An interior point algorithm for large-scale nonlinear optimization with applications in process engineering, Ph.D. thesis, Carnegie Mellon University (2002).

[59] K. E. Jensen, Anisotropic mesh adaptation and topology optimization in three dimensions, J. Mech. Design 138 (6) (2016) 061401–1–061401–8.

[60] M. Bruggi, M. Verani, A fully adaptive topology optimization algorithm with goal-oriented error control, Comput. Struct. 89 (2011) 1481–1493.

[61] L. Formaggia, S. Micheletti, S. Perotto, Anisotropic mesh adaption with application to CFD problems, in: H. Mang, F. Rammerstorfer, J. Eberhardsteiner (Eds.), Proceedings of WCCM V, Fifth World Congress on Computational Mechanics, 2002, pp. 1481–1493.

[62] L. Dedè, S. Micheletti, S. Perotto, Anisotropic error control for environmental applications, Appl. Numer. Math. 58 (9) (2008) 1320–1339.

[63] S. Micheletti, S. Perotto, P. E. Farrell, A recovery-based error estimator for anisotropic mesh adaptation in CFD, Bol. Soc. Esp. Mat. Apl. SeMA (50) (2010) 115–137.

[64] P. E. Farrell, S. Micheletti, S. Perotto, An anisotropic Zienkiewicz-Zhu-type error estimator for 3D applications, Int. J. Numer. Meth. Engng 85 (6) (2011) 671–692.

[65] M. Ainsworth, J. T. Oden, A Posteriori Error Estimation in Finite Element Analysis, John Wiley & Sons, New York, 2000.

[66] W. Bangerth, R. Rannacher, Adaptive Finite Element Methods for Differential Equations, Lectures in Mathematics ETH Zürich, Birkhäuser Verlag, Basel, 2003.

[67] R. Verfürth, A Review of A Posteriori Error Estimation and Adaptive Mesh-Refinement Techniques, Wiley & Teubner, 1996.

[68] O. C. Zienkiewicz, J. Z. Zhu, A simple error estimator and adaptive procedure for practical engineering analysis, Int. J. Numer. Meth. Engng 24 (1987) 337–357.

[69] O. C. Zienkiewicz, J. Z. Zhu, The superconvergent patch recovery and a posteriori error estimates. I: The recovery technique, Int. J. Numer. Meth. Engng 33 (1992) 1331–1364.

[70] O. C. Zienkiewicz, J. Z. Zhu, The superconvergent patch recovery and a posteriori error estimates. II: Error estimates and adaptivity, Int. J. Numer. Meth. Engng 33 (1992) 1365–1382.

[71] S. Micheletti, S. Perotto, Anisotropic adaptation via a Zienkiewicz-Zhu error estimator for 2D elliptic problems, in: G. Kreiss, P. Lötstedt, A. Målqvist, M. Neytcheva (Eds.), Numerical Mathematics and Advanced Applications, Springer-Verlag Berlin Heidelberg, 2010, pp. 645–653.

[72] P.-L. George, H. Borouchaki, Delaunay Triangulation and Meshing. Application to Finite Elements, Editions Hermès, Paris, 1998.

[73] C. Dapogny, C. Dobrzynski, P. Frey, Three-dimensional adaptive domain remeshing, implicit domain meshing, and applications to free and moving boundary problems, J. Comput. Phys. 262 (2014) 358–378.

[74] U. Ayachit, The ParaView Guide: A Parallel Visualization Application, Kitware, Inc., USA, 2015.

[75] A. Michell, The limits of economy of material in frame-structures, Philosophy Magazine 8 (1904) 589–597.

[76] T. Ferri, Topology and Shape Optimization for Structural Design, Master's thesis, Politecnico di Milano (2017).

MOX Technical Reports, last issues

Dipartimento di Matematica
Politecnico di Milano, Via Bonardi 9 - 20133 Milano (Italy)

57/2018 Ferro, N.; Micheletti, S.; Perotto, S.
POD-assisted strategies for structural topology optimization

56/2018 Antonietti, P.F.; Manzini, G.; Verani, M.
The conforming virtual element method for polyharmonic problems

54/2018 Dal Santo, N.; Deparis, S.; Manzoni, A.; Quarteroni, A.
Multi space reduced basis preconditioners for parametrized Stokes equations

52/2018 Possenti, L.; di Gregorio, S.; Gerosa, F.M.; Raimondi, G.; Casagrande, G.; Costantino, M.L.; Z
A computational model for microcirculation including Fahraeus-Lindqvist effect, plasma skimming and fluid exchange with the tissue interstitium

53/2018 Giantesio, G.; Musesti, A.; Riccobelli, D.
A comparison between active strain and active stress in transversely isotropic hyperelastic materials

55/2018 Cerroni, D.; Laurino, F.; Zunino, P.
Mathematical analysis, finite element approximation and numerical solvers for the interaction of 3D reservoirs with 1D wells

51/2018 Stella, S.; Vergara, C.; Giovannacci, L.; Quarteroni, A.; Prouse, G.
Assessing the disturbed flow and the transition to turbulence in the arteriovenous fistula

50/2018 Gervasio, P.; Quarteroni, A.
The INTERNODES method for non-conforming discretizations of PDEs

48/2018 Arnone, E.; Azzimonti, L.; Nobile, F.; Sangalli, L.M.
Modeling spatially dependent functional data via regression with di fferential regularization

47/2018 Stefanucci, M.; Sangalli, L.M.; Brutti, P.
PCA-based discrimination of partially observed functional data, with an application to Aneurisk65 dataset